11 Convective Mixed Layer

Buoyancy is the dominant mechanism driving turbulence in a convective boundary layer. Such turbulence is not completely random, but is often organized into identifiable structures such as thermals and plumes (Young, 1988). Entrainment happens at a variety of scales: lateral entrainment by small eddies into the sides of thermals, and vertical entrainment on the thermal scale into the whole mixed layer. In this chapter we examine the structure and evolution of the convective boundary layer, and study the forcings acting on it.

Three layers can be identified within the convective boundary layer (Driedonks and Tennekes, 1984) as shown in Fig 11.1:

(1) the surface layer in the bottom 5 to 10%,
(2) the mixed layer composing the middle 35 to 80%, and
(3) the entrainment zone in the top 10 to 60%.

In the unstable ***surface layer*** there are small-scale structures such as buoyant vertical plumes, convergence lines, sheets of rising air, and dust devils. Higher in the ***mixed layer*** we observe larger-diameter thermals, horizontal roll vortices, and mesoscale cellular convection patterns. In the ***entrainment zone*** at the top of the mixed layer we find intermittent turbulence, overshooting thermals, Kelvin-Helmholtz waves, internal gravity waves, and sometimes clouds. Often the whole convective boundary layer is called the mixed layer.

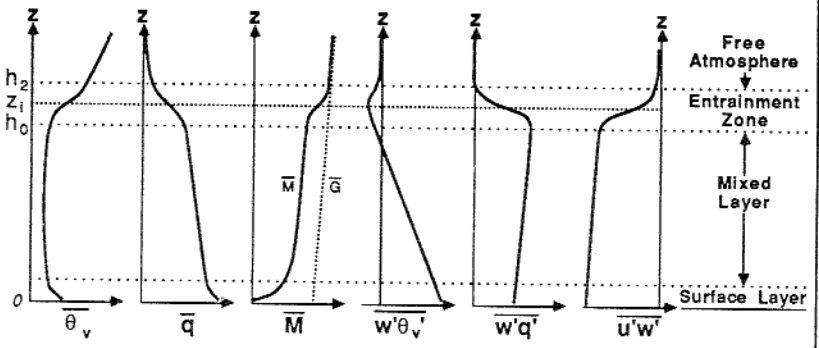

Fig. 11.1 Mean characteristics of layers within the convective boundary layer. (After Driedonks and Tennekes, 1984).

11.1 The Unstable Surface Layer

11.1.1 Mean Characteristics

The surface layer is characterized by a superadiabatic lapse rate, moisture decrease with height, and strong wind shear (see Fig 11.1) that are all well described by Monin-Obukhov similarity theory. The temperature and moisture at any height depend strongly on the recent history of the surface layer, and must be predicted using prognostic equations (Chapter 3) together with the initial and boundary conditions. Nevertheless, the shape (e.g., vertical gradients) of these profiles is quasi-steady, allowing diagnostic description using similarity theory (Chapter 9). The wind profile is not as dependent on the time history, because the wind speed is always zero at the surface, but it can be altered by a nonuniform bottom boundary (see Chapter 14). As a result, both the wind gradient and the mean wind profile itself can usually be described diagnostically by the log wind profile (Chapter 9).

The virtual potential temperature decreases very rapidly across the microlayer, from the relatively hot surface skin temperature to the warm temperatures at the bottom of the surface layer. In the remainder of the surface layer, the virtual potential temperature gradient decreases smoothly with height, becoming nearly zero at the top of the surface layer. The strong gradients in the microlayer support molecular conduction, as previously discussed, while the gradients in the remainder of the surface layer support down-gradient (small-eddy) turbulent diffusion. The gradient diffusion processes decrease in importance with height within the surface layer as large-eddy nonlocal transport and mixing take over.

Evaporation/transpiration from the surface occurs if the ground is moist and/or vegetated. The moisture gradient decreases with height in a manner similar to the temperature gradient, becoming relatively small at the top of the surface layer.

Strong convective mixing brings higher momentum air to the ground, where drag at the surface acts as a momentum sink. The mixing process is vigorous enough to maintain substantial wind speeds at the typical anemometer height of 10 m, in agreement with our casual observations that the surface winds are stronger during the day than at night over land. Superimposed on this mean wind profile is a gustiness associated with the passage of structures such as convergence lines and plumes.

In the next subsections we will explore some of the details of surface-layer structures. The structures examined here are those generated by heating at the bottom of the boundary layer, rather than by cooling at the top.

11.1.2 Plumes

Plumes are coherent vertical structures of warm rising air having diameters and depths on the order of the the surface layer depth — namely ~100 m. Above the surface layer, the plumes become more diffuse and appear to merge together to form the larger-diameter (order of 1 km) mixed-layer thermals. Some studies indicate that plumes occupy an average of about 42% of the horizontal area, with weak cool downdrafts between them. Fig 11.2 shows a sketch of an idealized plume and identifies its components (Kaimal and Businger, 1970; Wilczak and Tillman, 1980; Wilczak, 1984).

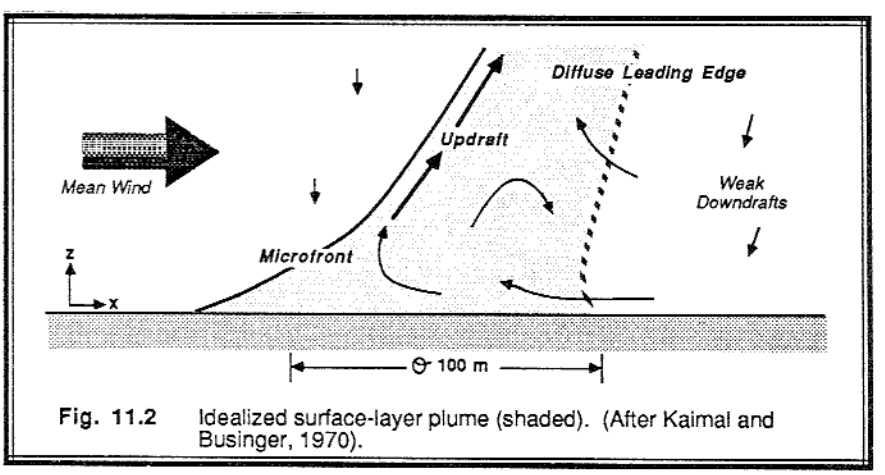

Fig. 11.2 Idealized surface-layer plume (shaded). (After Kaimal and Businger, 1970).

Even though buoyancy is the dominant forcing, the ambient mean wind modifies the plume structure so that the leading edge is diffuse and the trailing edge is sharp. The trailing edge is called the ***microfront***. Plumes translate horizontally with a speed equal to the mean wind speed averaged over their depth. Thus, the plumes translate horizontally at a speed faster than the surface wind speed, but slower (70-80%) than the mean mixed layer wind.

Wind shear causes the plumes to tilt in the down shear direction at an inclination angle of about 45°. The tilt is relatively constant with time in spite of the shear, but the plume is

more vertical when the shear is weak and the buoyancy strong. For weak convection and strong winds, plumes are elongated in the along-wind direction with an aspect ratio of approximately 8:1. Lengths of hundreds of meters (e.g., 500 m) and widths of tens of meters are typical in strong winds. In weak winds and strong convection, the opposite pattern occurs, with elongation in the the cross-wind direction, contraction in the along-wind direction, and a meandering propagation like a miniature front.

When a plume moves past a fixed mast or tower, the resulting temperature trace shows a characteristic ***ramp structure*** or sawtooth shape close to the surface, as sketched in Fig 11.3. The diffuse leading edge marks the start of the warming temperatures in the ramp, while passage of the trailing microfront results in a sharp 1-2°C drop in temperature back to the surrounding environmental values. Higher in the surface layer (above about 30 m), the microfront becomes more diffuse and the temperature excess in the plume becomes smaller.

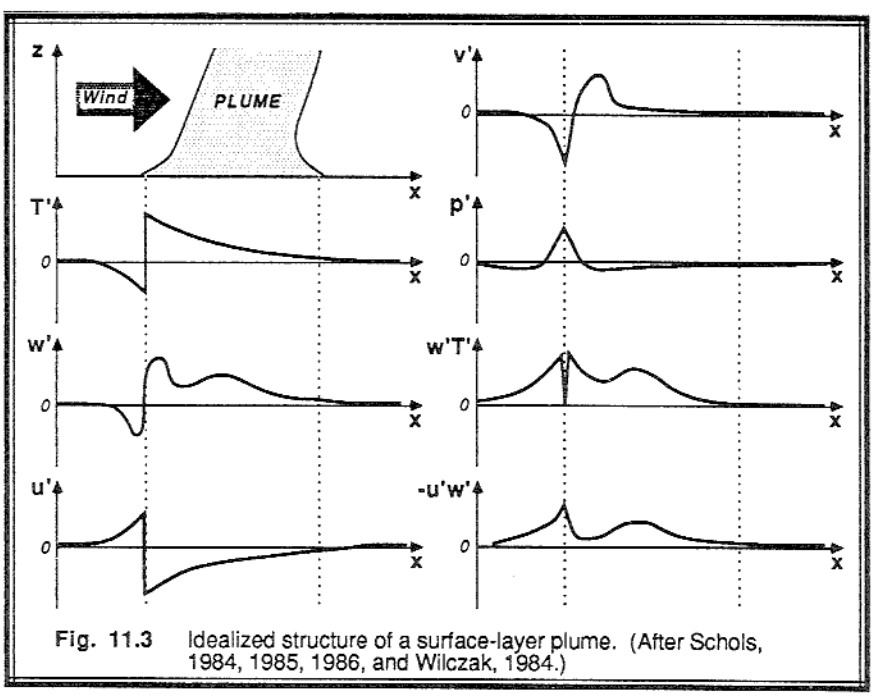

Fig. 11.3 Idealized structure of a surface-layer plume. (After Schols, 1984, 1985, 1986, and Wilczak, 1984.)

Air within a plume accelerates upward due to its buoyancy, leading to average vertical velocities of about 1 m/s. The vertical acceleration helps prevent the plume from increasing its tilt within the sheared environment of the surface layer. Air in the ramp is more turbulent than the surrounding descending air, resulting in vertical velocity fluctuations of on the order of 5 m/s in the ramp. In fact, in some random spots within the ramp the vertical velocity is downward.

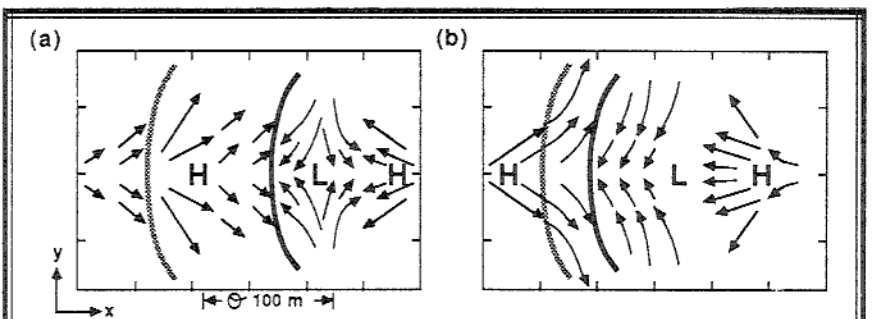

Fig. 11.4 (a) Schematic of the circulation pattern in a horizontal plane at -z/L≈2 after subtracting the mean wind. Regions of high (H) and low (L) pressure are indicated. (b) As in (a) except at -z/L≈0.5. The microfront is shown aloft and at the surface with the heavy solid and shaded lines, respectively. (After Wilczak, 1984).

Idealized horizontal and vertical circulation patterns, ensemble averaged over many ramp structures, are sketched in Fig 11.4. High perturbation pressures at the surface below the downdraft regions are associated with divergent horizontal circulations, while beneath the plume updraft there is convergence and a surface low.

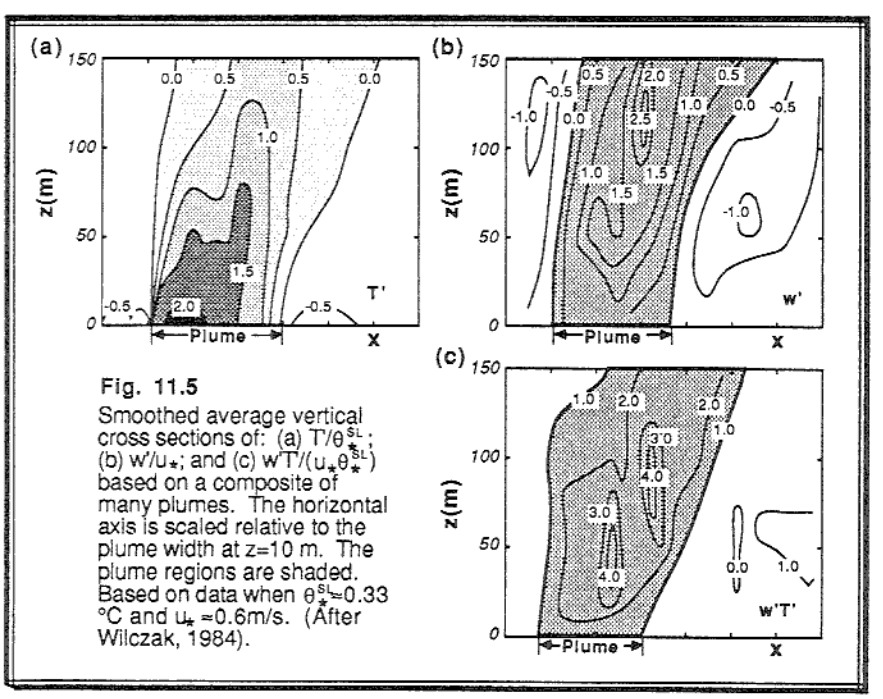

Fig. 11.5
Smoothed average vertical cross sections of: (a) T'/θ_*^{SL}; (b) w'/u_*; and (c) $w'T'/(u_*\theta_*^{SL})$ based on a composite of many plumes. The horizontal axis is scaled relative to the plume width at z=10 m. The plume regions are shaded. Based on data when θ_*^{SL}≈0.33 °C and u_* ≈0.6m/s. (After Wilczak, 1984).

We can envision the plume as analogous to a vacuum cleaner that propagates horizontally faster than the mean surface wind, and "peels up" warm surface-layer air into the trailing edge of the plume. Similar processes have been suggested for the inflow and ramp structure in small cumulus clouds (Telford, 1986). Most of the turbulent heat flux happens near the trailing edge of the plume. Fig 11.5 shows highly smoothed vertical cross sections of the temperature, velocity, pressure, and fluxes within a plume.

The picture imagined above applies only to convection over a uniform surface. Surface inhomogeneities that are hotter than average (asphalt parking lots or dark plowed fields) or taller than average (hills, tree lines, hedge/fence lines, dikes) can trigger plumes. Glider pilots look for these favored areas for enhanced lift.

One last caution about the word "plume". For air pollution and diffusion the word "plume" usually refers to a quasi-horizontal smoke plume downwind of an emission source. This can get confusing, because the dispersion of smoke plumes in the surface layer depend on the quasi-vertical buoyant plume structures just defined.

11.1.3 Surface Convergence Bands and Updraft Curtains

The unaided eye can detect microfronts and surface convergence bands from "cats paws" on lakes, observed variations in precipitation densities, steam fog patterns, blowing leaves and dust, and wavy fields of grain. Quantitative measurements of surface convergence bands have been made with Doppler radar (Kropfli, 1979).

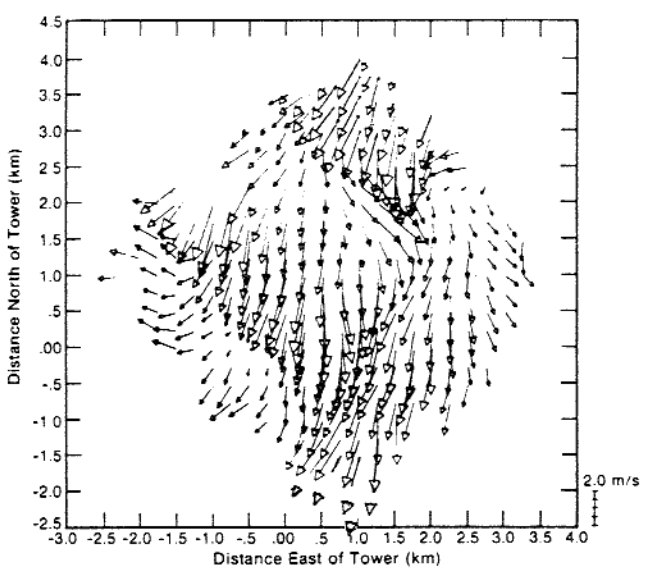

Fig. 11.6 Horizontal eddy wind fields (volume mean removed) for z=0.1 km at 1531 MDT. (After Kropfli, 1979).

Fig 11.6 shows one example, where the volume-mean wind has been subtracted. Horizontal convergence patterns resembling "fish nets" or "honeycombs" can be seen in the flow. The scale of the cell size in the net is about 2 km for this case, suggesting that these surface patterns are artifacts of mixed-layer thermals rather than surface-layer plumes. Other examples not shown here suggest surface layer scales, with pattern cell dimensions on the order of hundreds of meters.

In these fish net patterns we can see lines of enhanced convergence. Above these lines it is likely that there exist sheets or ***updraft curtains*** of rising buoyant air. These updraft curtains might be one realization of the elongated plumes described earlier. At the intersection of these curtains (i.e., at the knots in the fish net) we would expect to find enhanced buoyancy and rising motion. Although it is difficult to study directly, we can infer that a number of these curtains merge to form the larger-diameter thermals in the mixed layer.

Young (1988) points out the similarity of surface layer structures to the corresponding entrainment structures at the top of the mixed layer. Namely, updraft curtains in the surface layer merge to form larger more diffuse updrafts, while entrained downdraft curtains in the entrainment zone become more diffuse mixed-layer downdrafts. Together, these structures can be envisioned as sketched in Fig 11.7.

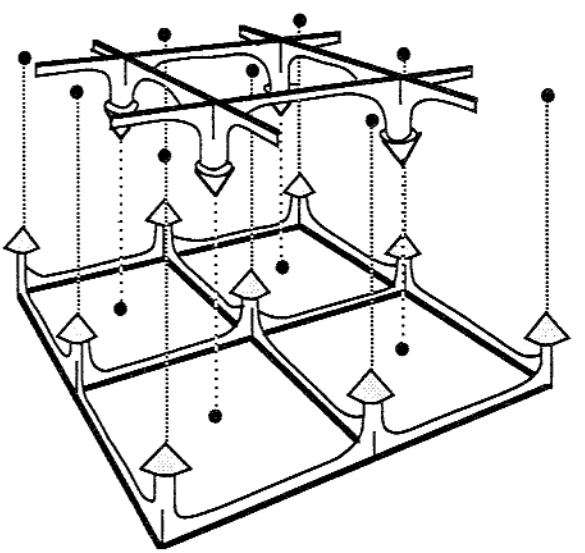

Fig. 11.7 Idealization of the similarity between plumes rising from the bottom of the ML and entrained air descending from above. (After Young, 1988).

Convergence and divergence can be measured using the inflow rate across the boundaries of known areas. For example, laser scintillation sensors were arranged in a

triangle that was 450 m on a side, with each sensor 4 m above the ground during the PHOENIX experiment (Fritz and Wang, 1979). This "optical" triangle, centered on the BAO tower, measured convergence as shown in Fig 11.8a. The short-period oscillations in convergence are probably correlated with plume structures, and agree fairly well with the vertical velocities measured at the 100 m height on the tower (Fig 11.8b).

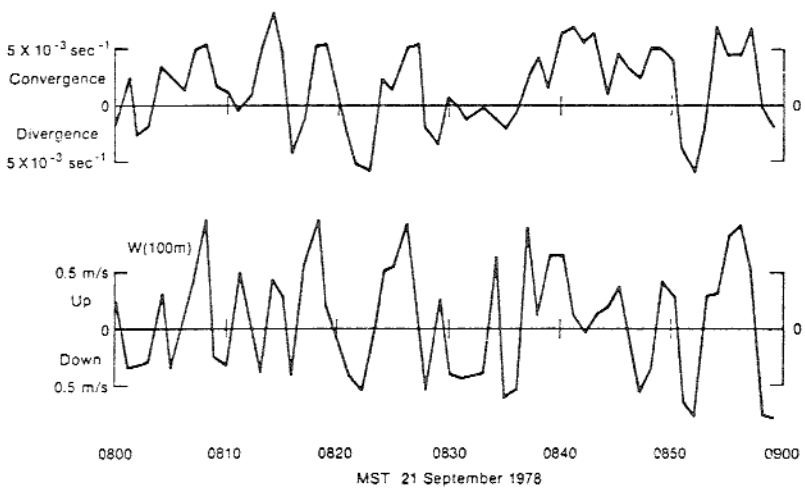

Fig. 11.8 Time series of divergence from a small optical triangle compared with vertical velocity fluctuations recorded at the 100 meter level of the BAO tower. (After Fritz and Wang, 1979).

11.1.4 Dust Devils

Dust devils are rotating updrafts of buoyant air that frequently form in fair weather conditions (Fitzjarrald, 1973; Golden, 1974; Idso, 1975a,b,c; Kaimal and Businger, 1970, News and Notes, 1976; Sinclair, et al., 1977). They are not necessarily associated with clouds, and are not related to tornadoes or water spouts. Tangential velocities in dust devils are on the order of 10 m/s, compared to 50 m/s for water spouts and 100 m/s for tornadoes. Diameters of the order of tens of meters, and depths of about 100 m are typical.

Dust devils are visible to the naked eye because the tangential velocities are sufficient to pick up dust from the ground, and vertical velocities on the order of 4 m/s can carry the finer dust aloft. Close cousins are ***steam devils***, formed in steam fog regions of cold air advection over warm bodies of water or other moist surfaces, and ***ash devils***, formed over ground covered by volcanic ash. There is evidence that dust devils form

almost as often over nondusty ground, although the absence of dust makes them invisible to the eye. Dust devils form in the same general conditions as plumes and coexist with them, but are only about 10% as numerous.

Fig 11.9 shows the circulations structure of an idealized dust devil (Sinclair, et al., 1977). A weak downdraft with vertical velocities on the order of 2 m/s in the center of the dust devil is usually less dusty than the surrounding vortex, and is often visible to the eye. The dust devil is approximately cylindrical, and is tilted with the ambient shear. Like the plume, it translates at a speed equal to the wind speed averaged over its depth, and thus moves faster than the surface wind. Although it occurs less frequently than the plume, it transports about ten times the vertical heat flux (Kaimal and Businger, 1970).

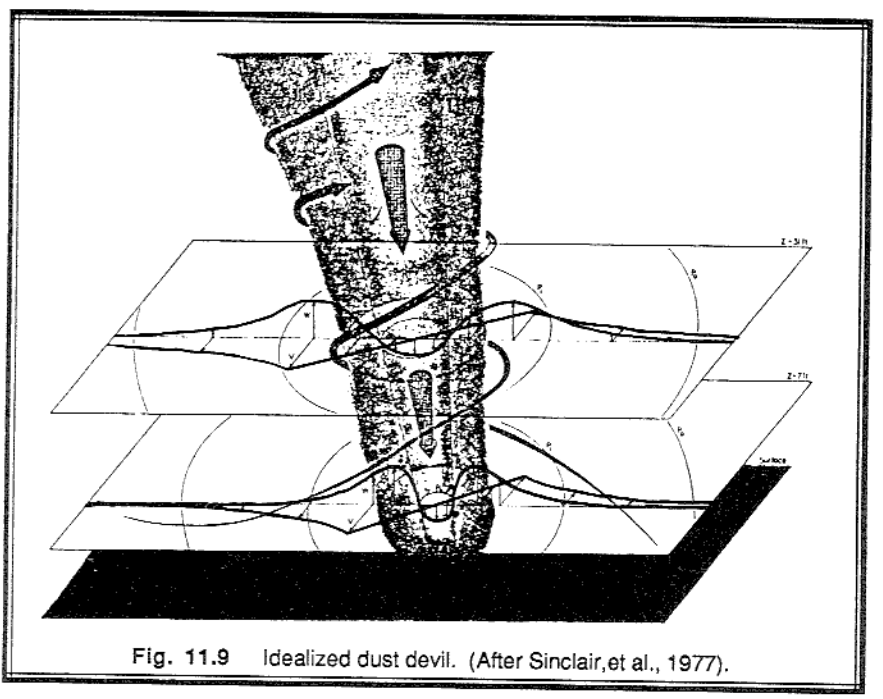

Fig. 11.9 Idealized dust devil. (After Sinclair,et al., 1977).

It has been suggested that a certain critical tangential velocity is needed to allow the dust devil to persist against the disruptive action of turbulence. These critical vorticities can sometimes be achieved by eddies generated by the mean wind flowing around obstacles. It is also possible that chance occurrences of vorticity in the mean flow are enhanced by vortex line stretching in plume updrafts. No favored direction of rotation in dust devils has been noted.

11.2 The Mixed Layer

11.2.1 Mean Characteristics

Profile Shapes. The mixed layer (ML) is so named because intense vertical mixing tends to leave conserved variables such as potential temperature and humidity nearly constant with height (see Fig 11.1). Even wind speed and direction are nearly constant over the bulk of the mixed layer. Sometimes the mixed layer is called the ***well-mixed layer***.

The top of the whole convective mixed layer, z_i, is often defined as the level of most negative heat flux. This level is near the middle of the entrainment zone, often at the height where the capping inversion is strongest (see Fig 11.1). The capping inversion acts like an interface between the ML and the FA. Another measure of the average ML depth is the height at which an undiluted air parcel rising from the surface becomes neutrally buoyant.

Mixing can be generated mechanically by shears, or convectively by buoyancy. Buoyantly generated MLs tend to be more uniformly mixed than ones driven mechanically, because anisotropy in convection favors vertical motions, while shear anisotropy favors horizontal motions. Shears near the ground are usually more important for generating mixing than shears across the top of the ML, for atmospheric situations. Shears at the ML top, however, can cause a separate layer to form. A mixed layer dominated by buoyant turbulence generation is called a ***convective boundary layer (CBL)*** or ***convective mixed layer***.

Looking more closely at the conserved variables, we find that they are not quite uniform in the vertical, because the mixing process is not instantaneous and because mixing is partially counteracted by forcings acting on the top and bottom of the ML. Potential temperature, for example, is a minimum near the middle of the ML, because heating from below and entrainment of warm air from above lead to slightly warmer potential temperatures in those regions. Moisture, however, often decreases slightly with height, because surface evaporation is adding moisture below, while entrainment of dry air is occurring at the top of the ML.

Equilibrium. The convective time scale, t_*, is on the order of 10-20 minutes in many cases. This is the typical time period for air to circulate between the surface and the top of the ML. Thus, changes in surface heat flux and other surface forcings can be communicated to the rest of the ML in a relatively short time — about 15 minutes.

As discussed in the next subsection, the ML depth changes relatively slowly in the early morning and in the afternoon. During these periods the ML is in a state of ***quasi-equilibrium***, because of the short convective time scale. Similarity theory works well for these cases.

Conservation Equations. Let the angle brackets $< >$ denote an average of any quantity, ξ, over the depth of the mixed layer:

$$\langle \xi \rangle \equiv \frac{1}{z_i} \int_{z=0}^{z_i} \xi \, dz \qquad (11.2.1a)$$

One can integrate the conservation equations (3.5.3) to yield:

$$z_i \frac{d\langle \bar{\theta} \rangle}{dt} = \overline{w'\theta'}_s - \overline{w'\theta'}_{z_i} \qquad (11.2.1b)$$

$$z_i \frac{d\langle \bar{q} \rangle}{dt} = \overline{w'q'}_s - \overline{w'q'}_{z_i} \qquad (11.2.1c)$$

$$z_i \frac{d\langle \bar{U} \rangle}{dt} = \overline{w'u'}_s - \overline{w'u'}_{z_i} - f_c \langle \overline{V}_g - \overline{V} \rangle z_i \qquad (11.2.1d)$$

$$z_i \frac{d\langle \bar{V} \rangle}{dt} = \overline{w'v'}_s - \overline{w'v'}_{z_i} + f_c \langle \overline{U}_g - \overline{U} \rangle z_i \qquad (11.2.1e)$$

where body source terms have been neglected. Note that the only fluxes that are important are those at the top and bottom of the ML. The flux at the bottom is usually specified as a boundary condition, while the flux at the top can be found from $\overline{w'\xi'} = -w_e(\bar{\xi}_{z_i^+} - \langle \bar{\xi} \rangle)$ if the entrainment velocity is known. To complete this set of equations we need the continuity equation, which depends on the evolution of the ML described next.

11.2.2 Evolution

Phases. Growth of the ML depth during a diurnal cycle is often a 4-phase process:

(1) Formation of a shallow ML, which slowly deepens
(2) Rapid ML growth
(3) Deep ML of nearly constant thickness
(4) Decay of turbulence

Fig 11.10 shows an example of the first three phases as measured by a ground-based lidar (Wilde, et al., 1985).

During the early morning the mixed layer is shallow, starting with a depth on the order of tens of meters for calm situations to depths of a couple hundred meters for windier situations. Its depth increases slowly at first because of the strong nocturnal stable layer that caps the young ML. This first phase is sometimes referred to as the ***burning off*** of the nocturnal inversion.

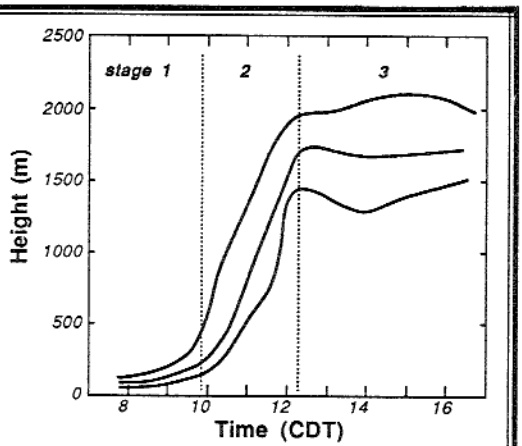

Fig. 11.10
Evolution of the entrainment zone measured by lidar at the BLX83 field site for 15 June 1983. The top and bottom lines represent the top and bottom of the entrainment zone, respectively, while the middle line is the average, mixed layer depth, $\overline{z_i}$. (After Wilde, et al., 1985.)

By late morning, for many cases, the cool nocturnal air has been warmed to a temperature near that of the residual layer, and the top of the ML has moved up to the residual-layer base. Since there is virtually no stable layer capping the ML at this point, the thermals penetrate rapidly upward during the second phase, allowing the top of the mixed layer to rise at rates of up to 1 km per 15 minutes.

When the thermals reach the capping inversion at the top of the residual layer, they meet resistance to vertical motion again and the ML growth rate rapidly decreases. During this third phase the ML depth is relatively constant during most of the afternoon. Slow depth changes are related to the balance between entrainment and subsidence. These final depths vary widely from place to place, depending on synoptic and mesoscale conditions. Final depths of 400 m have been observed over some tropical ocean regions, while depths in some desert areas reach 5 km. Typical depths over land in mid-latitudes are on the order of 1 to 2 km.

As the sun sets, the generation rate of convective turbulence decreases to the point where turbulence can not be maintained against dissipation (Nieuwstadt and Brost, 1986). In the absence of mechanical forcings, turbulence in the ML decays completely, causing us to reclassify that layer as a residual layer. Temperature fluctuations decay the fastest, while TKE decays more slowly. During this decay process the last few weak thermals may still be rising in the upper part of the ML and can still cause entrainment, while the surface layer has already become stably stratified (Stull and Driedonks, 1987). Thermals and other eddies formed as the surface heating approaches zero appear to scale to the time scale, t_*, that existed at the time of thermal creation, resulting in a possible decoupling of large and small scales (e.g., old thermals vs. new shear eddies) and a failure of similarity theory.

Turbulent Entrainment and Mixed-Layer Growth. During free-convection, buoyant thermals from the surface layer gain momentum as they rise through the ML. Upon reaching the warmer free atmosphere they find themselves negatively buoyant, but

overshoot a short distance because of their momentum (Fig 11.11). This overshooting is called ***penetrative convection*** (Deardorff, et al., 1969). The tops of the overshooting thermals form dome or hummock-like structures. There is little ambient turbulence in the FA, and hence no way to disperse air from the overshooting thermal into the rest of the free atmosphere. The negatively-buoyant thermal sinks back down into the ML mostly intact. Any pollutants from the ML return to, and are trapped within, the ML.

During the overshoot into the inversion, wisps or sheets or curtains of warm FA air are pushed into the ML. These curtains become rapidly mixed down into the ML because of the strong turbulence there, and do not return up to the capping stable layer in spite of their positive buoyancy. The net result is entrainment of FA air into the ML. Thus, the ML grows in thickness due to a ***one-way entrainment process: less turbulent air is entrained into more turbulent air.*** Thus, the ML erodes into the FA. The ML can never become shallower by entrainment.

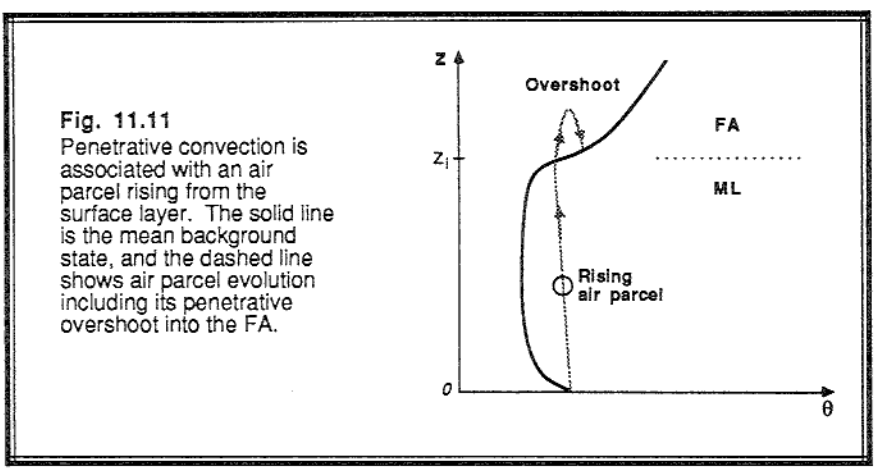

Fig. 11.11
Penetrative convection is associated with an air parcel rising from the surface layer. The solid line is the mean background state, and the dashed line shows air parcel evolution including its penetrative overshoot into the FA.

The volume of air entrained into the top of the ML per unit horizontal area per unit time (i.e., the volume flux) has the same units as velocity, and is called the entrainment velocity, w_e. This velocity is governed by the turbulence intensity and the strength of the capping inversion. Several parameterizations for the entrainment velocity are given in Section 11.4.

Continuity Equation. To first order, air density in the mixed layer can be assumed constant, allowing us to use volume conservation in place of mass conservation. In a column of ML air over a given area, A, on the earth, the volume is $A \cdot z_i$. If η represents the net volumetric flow rate into the volume, then volume conservation yields:

$$A \frac{dz_i}{dt} = \eta$$

Inflow can occur in the vertical because of entrainment at the top of the ML, and in the horizontal because of convergence within the ML:

$$\eta = w_e A - \int_{z=0}^{z_i} \iint_A \text{Div}\ dx\, dy\, dz$$

where Div is the horizontal divergence.

The last term on the right can be integrated and rewritten in terms of the mean large-scale vertical motion, w_L, acting at the top of the ML (i.e., subsidence). Upon combining the above two equations and dividing by A, we find:

$$\frac{dz_i}{dt} = w_e + w_L \qquad (11.2.2a)$$

where w_L is negative for subsidence. When active clouds are present that vent air out of the top of the ML, the volume conservation equation can be rewritten as (Stull, 1985):

$$\frac{dz_i}{dt} = (1 - \sigma_A)\, w_e - \sigma_A\, w_c + w_L \qquad (11.2.2b)$$

where σ_A is the fraction of sky covered by active clouds, and w_c is the average vertical velocity (positive upward) within the clouds at height z_i.

When there are no clouds and no subsidence, (11.2.2a) shows that the mixed layer top rises at a rate equal to w_e. Subsidence can reduce the rise rate, or even push the ML down. Subsidence, however, can never inject air into the ML, because entrainment is controlled by w_e. In convergent situations, the ML top can rise much faster than w_e. Also, the total derivatives on the left side of both equations above can be split into local derivative and advective parts. Thus, advection of higher or lower ML depths into a region contribute to the local change, and should not be neglected.

Thermodynamic (Encroachment) Mixed-Layer Growth. One of the simplest ways to forecast ML depth and temperature is to focus only on the thermodynamics, and neglect the dynamics of turbulent entrainment. For example, consider the early morning potential temperature sounding sketched in Fig 11.12a. If later in the morning the temperature reaches a value θ_1, then the mixed layer depth at that time is z_{i1}, assuming that the potential temperature within the whole mixed layer is constant with height. The amount of heat needed to reach this state is indicated by the shading in Fig 11.12a, and is given in units of K·m. Obviously more heat is required to reach a deeper ML depth with a warmer ML temperature.

Given a sensible heat flux curve such as shown in Fig 11.12b, we know that the amount of heat supplied to the air by time t_1 is shown by the area shaded under that curve. Thus, a simple graphical method for estimating ML depth at time t_1 is (1) find the area under the heat flux curve up to that time; (2) estimate what adiabat under the early morning sounding corresponds to the same amount of heating; and (3) determine the ML depth as the height where the adiabat intercepts the morning sounding. This approach for estimating the ML depth is called the ***thermodynamic method***, and it neglects factors such as advection or subsidence which might alter the sounding during the day.

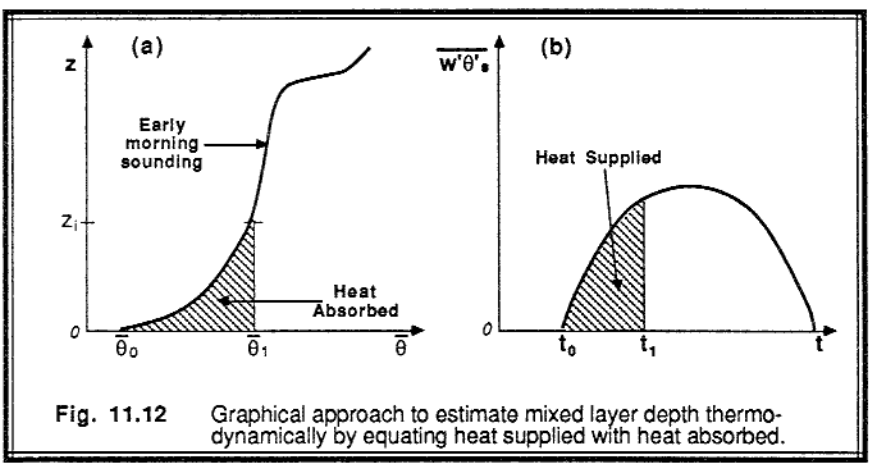

Fig. 11.12 Graphical approach to estimate mixed layer depth thermodynamically by equating heat supplied with heat absorbed.

The same result is obtained by neglecting advection, radiation, and latent heating, and then integrating the heat conservation equation (3.5.3f) over height and time, and using the chain rule:

$$\int_{t=0}^{t_1} \overline{w'\theta'}_s(t)\, dt \quad = \quad \int_{\theta=\theta_o}^{\theta_1} z(\theta)\, d\theta \qquad (11.2.2c)$$

where $z(\theta)$ represents the early morning sounding. Knowing t_1, this equation can be integrated and solved for θ_1, which is then used in the sounding to estimate the ML depth: $z_{i1} = z(\theta_1)$.

An equally-valid approach utilizes the local lapse rate of the morning sounding above the current top of the ML:

$$\frac{\partial z_i}{\partial t} \quad = \quad \frac{1}{\gamma} \frac{\partial \langle \bar{\theta} \rangle}{\partial t} \qquad (11.2.2d)$$

where γ is the local value of $\partial\overline{\theta}/\partial z$ just above the top of the ML, and where $<\overline{\theta}>$ is the potential temperature vertically averaged over the ML depth. When this is combined with (11.2.1b), the result is a prognostic equation for z_i:

$$\frac{\partial z_i}{\partial t} = \frac{\overline{w'\theta'}_s - \overline{w'\theta'}_{z_i}}{\gamma \; z_i} \tag{11.2.2e}$$

For the special case of constant heat flux with time, and constant lapse rate with height, (11.2.2e) can be integrated to yield:

$$z_i^2 - z_{i_o}^2 = \frac{2}{\gamma}\left[\overline{w'\theta'}_s - \overline{w'\theta'}_{z_i}\right] \cdot (t - t_o) \tag{11.2.2f}$$

which shows that the ML depth could increase with the square root of time for this special case. Sometimes, a complex sounding can be broken into segments and integrated piece by piece using (11.2.2f).

If one assumes that heating from the surface is the sole source of warming of the ML, then the heat flux at z_i is assumed to be zero in (11.2.2e-f). This special case is called ***encroachment***, because the top of the ML is never higher than the intercept of the ML potential temperature with the early morning sounding. The ML encroaches upward only as the ML warms.

Even though the thermodynamic approach neglects turbulent entrainment, it explains roughly 80-90% of the observed variation of the ML depth (Stull, 1976; Boers, et al., 1984). One reason is that if turbulent entrainment "gets ahead" of the thermodynamic support, the temperature inversion at the top of the ML will intensify and limit the entrainment rate (see Section 11.4).

11.2.3 Models

Bulk Model. The simplest representation of the ML assumes that mean variables are constant with height within the ML, with a sharp discontinuity between the ML and the FA. This idealization is sometimes called a ***bulk or slab model*** because the ML is represented by a uniform slab of air, or a ***jump model*** because of the discontinuity or step across the top. Another name used in the literature is ***integral model***. Fluxes within the ML are assumed to be linear with height, with a jump at the top (Fig 11.13). The entrainment zone is assumed to be infinitesimally thin.

Since the actual values of mean variables in the ML are identically equal to their vertical averages, the conservation equations assume a particularly simple form:

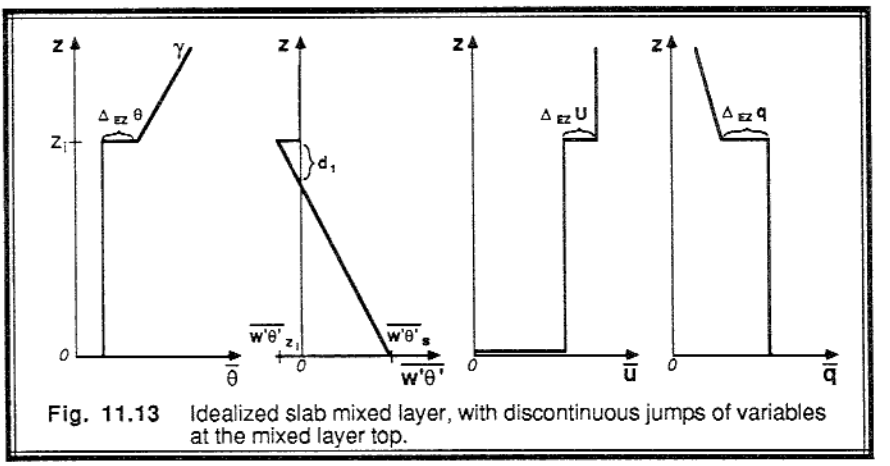

Fig. 11.13 Idealized slab mixed layer, with discontinuous jumps of variables at the mixed layer top.

$$z_i \frac{d\bar{\theta}}{dt} = \overline{w'\theta'}_s - \overline{w'\theta'}_{z_i} \qquad (11.2.3a)$$

with similar equations for humidity and winds. Above the ML the mean variables are assumed to change only by horizontal advection and subsidence.

For the sake of completeness, two other governing equations are rewritten here; the continuity equation (11.2.2a) and the equation for transport across an interface (7.4.3a):

$$\frac{dz_i}{dt} = w_e + w_L \qquad (11.2.3b)$$

$$\overline{w'\theta'}_{z_i} = - w_e \Delta_{EZ}\bar{\theta} \qquad (11.2.3c)$$

where $\Delta_{EZ}\bar{\theta} = \bar{\theta}_{z_i+} - \bar{\theta}_{ML}$ is the temperature jump across the entrainment zone at the top of the ML. Looking at the geometry of the idealized temperature profile, we expect the temperature jump to decrease as the ML warms, and to increase as entrainment eats upward into the warmer air (Tennekes, 1973):

$$\frac{d\Delta_{EZ}\bar{\theta}}{dt} = \gamma w_e - \frac{\partial\bar{\theta}}{\partial t} \qquad (11.2.3d)$$

If γ, w_L, and $\overline{w'\theta'}_s$ are specified as boundary conditions, then the above four equations contain five unknowns: z_i, $\bar{\theta}$, $\overline{w'\theta'}_{z_i}$, $\Delta_{EZ}\bar{\theta}$, and w_e. To close this set of equations, we must make a closure assumption or parameterization for one of the unknowns. As will be described in Section 11.4, some investigators make assumptions for w_e, while others make them for $\overline{w'\theta'}_{z_i}$. Recall that this approach can be categorized as half-order closure, because the shape of the mean profiles are fixed in advance, and only one integrated value for each variable is forecast in the ML.

The slab ML model has been used in oceanography and meteorology for a long time (Ball, 1960; Kraus and Turner, 1967; Lilly, 1968; Kraus, 1972; Stull, 1973; Betts, 1973; Tennekes, 1973), and continues to be a popular approach. Kraus and Leslie (1982), for example, have used coupled ocean and atmospheric slab mixed layers to study air-mass modification and stratus formation. Brutsaert (1987) studied ML drying associated with entrainment of dry air.

Higher-Order Local Closure. Higher-order local closure models (one-and-a-half through third order) have been very successful. Advantages of these higher-order models include being able to forecast TKE, variances, and fluxes (if using the second and higher order models). Examples and figures of ML forecasts made with these models have already been shown in Chapter 6.

Top down / bottom up (TDBU) Diffusion. As discussed earlier, K-theory (first-order local closure) often has difficulties in the mixed layer. Specifically, infinite values of the eddy diffusivity are required to maintain fluxes in the absence of mean gradients, and negative diffusivities are needed for counter-gradient fluxes.

One attempt to circumvent this dilemma while continuing to use first-order local closure is to study the mixing upward from the ground separately from the mixing downward from the top of the ML (Wyngaard and Brost, 1984; Moeng and Wyngaard, 1984; Wyngaard, 1987; Fairall, 1987; Young, 1988). For example, if one injects a red tracer into the bottom of the ML and a green tracer into the top, we would expect the red to disperse upward (down the red gradient) independent of the green concentration, and the green to disperse downward (down the green gradient) independent of the red concentration. The superposition of the red and green should not affect the the dispersion of either one.

If we instead inject a red tracer at both the top and bottom of the ML, the dispersion should be the same as the previous case. Thus, some of the red dispersing upward will do so counter to the gradient of red diffusing down, and vise versa. The strict formulation of the TDBU model requires the use of artificial gradient functions to allow separate down-gradient diffusion from both the top and bottom of the ML. As Young (1988) points out, however, there are still problems because the gradient functions cross zero and become negative, implying counter-gradient diffusion.

Nevertheless, we can use the results of TDBU to help explain the difference in profile shape of any mean ML variable, $\bar{\xi}$, from its idealized slab shape:

$$\bar{\xi}(z) = 0.8 \frac{\overline{w'\xi'}_s}{w_*} \left(\frac{z}{z_i} \right)^{-1/2} - 2.0 \frac{\overline{w'\xi'}_{z_i}}{w_*} \left(1 - \frac{z}{z_i} \right)^{-1/2} + \text{const.} \qquad (11.2.3e)$$

The vertical gradient of this function was already presented in Section 9.6.

The shape of this profile depends on both the surface flux and the entrainment flux (Fig 11.14). When the entrained flux is negative and the surface flux is positive, as it is for potential temperature, the mean profile of potential temperature is slightly concave to the right, with a stronger negative gradient near the surface and positive gradient near the ML top. For variables such as humidity that often have positive fluxes at both the top and bottom of the ML, the mean humidity profile exhibits a tilt with enhanced curvature at the top and bottom. The ratio of top to bottom fluxes, A_R, provides one measure of the overall shape (see Fig 11.14).

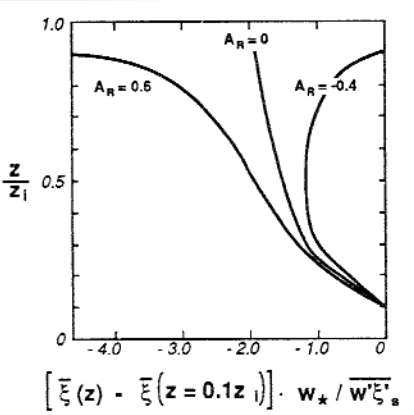

Fig. 11.14
Shape of the profile of any variable, $\bar{\xi}$ in the mixed layer as a function of the flux ratio, $A_R = \overline{w'\xi'}_{z_i} / \overline{w'\xi'}_s$. (After Wyngaard and Brost, 1984).

The mean gradients across the whole ML can also be related to the relative contributions of top and bottom fluxes (Mahrt and André, 1983; Driedonks and Tennekes, 1984):

$$\bar{\xi}_{z_i} - \bar{\xi}_s = -1.7 \frac{\overline{w'\xi'}_s}{w_*} - 5 \frac{\overline{w'\xi'}_{z_i}}{w_*} \qquad (11.2.3f)$$

Although the equation above gives approximate agreement with observed profiles, there is quite a lot of scatter in the data and uncertainty in the precise values of the two constants.

Transilient Models. Fiedler (1984) demonstrated that the TDBU model can be considered to be a special case of the non-local transilient closure model. Since the transilient approach explicitly models eddies mixing across finite distances, it can easily model the mixing associated with thermals rising in the ML. Local gradients are not used. Instead, differences between moving parcels and the surrounding environment determine the amount and direction of mixing.

Fig 11.15 shows a simulation of ML evolution observed near the Cabauw tower (Stull and Driedonks, 1987). The subset of grid points that were turbulent in this 1-D transilient model are shaded in the figure, and indicate the whole turbulent domain including the entrainment zone. Other measures of ML depth, namely the height at which a parcel rising from the surface would first become neutrally buoyant, and the height of most negative heat flux, are both indicated. The four phases of ML evolution are evident in this figure.

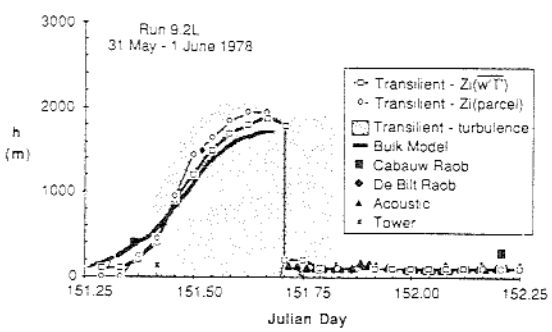

Fig. 11.15 Comparison of transilient modeled and observed boundary-layer depth for Cabauw, during 0600 UTC 31 May to 0600 UTC 1 June, 1978. (After Stull and Driedonks, 1987).

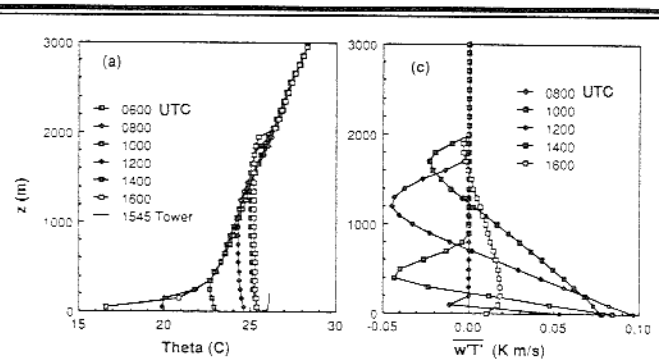

Fig. 11.16 Transilient simulations of the evolution of potential temperature and heat flux during the daytime hours of the same case as the previous figure. (After Stull and Driedonks, 1987).

The corresponding potential temperature and heat flux profiles are shown in Fig 11.16. Evident are the curvature of the potential temperature profiles, and the nearly linear heat flux profiles. On this day there were significant mechanical contributions to turbulence in addition to the dominant buoyant contributions. Heating of the lowest grid point by surface fluxes generated buoyant instabilities, to which the transilient model responded by generating mixing and producing a ML, as shown in the figures here and discussed in Chapter 6.

11.2.4 Thermal Structures

Thermals are large columns of rising buoyant air in the convective mixed layer (Fig 11.17). The convective circulation, including both the thermal updraft and associated downdraft, have horizontal scales of roughly 1.5 z_i (Caughey and Palmer, 1979; Young, 1988). Thus, early morning thermals are on the order of 100 m in diameter, while by late afternoon when the mixed layer is deeper thermals can be 1 to 2 km in diameter. The vertical extent of a thermal is also roughly equal to the ML depth.

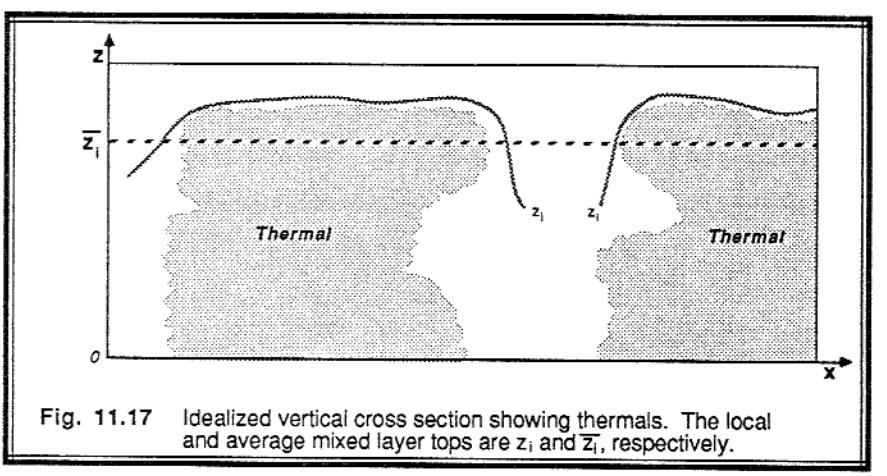

Fig. 11.17 Idealized vertical cross section showing thermals. The local and average mixed layer tops are z_i and $\overline{z_i}$, respectively.

Vertical velocities in thermals can reach 5 m/s or more, although weaker updrafts of 1 to 2 m/s are more common. Velocities scale to the convective velocity scale, w_*. Samples of vertical velocity (Caughey, et al., 1983; Deardorff and Willis, 1985) measured both in and between thermals typically show a negatively skewed distribution in the bulk of the ML (Fig 11.18), although the distributions tend to become more symmetric in the entrainment zone. There are a large number of weak interthermal downdrafts, and a small frequency of strong thermal updrafts. In a very idealized sense, this is pictured (Fig 11.19) as broad regions of gentle downdraft surrounding smaller regions of strong updraft.

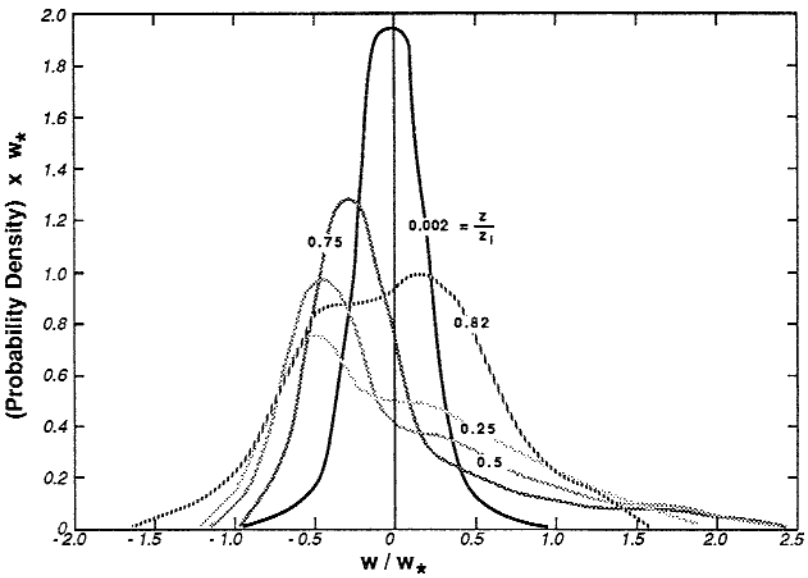

Fig. 11.18 Probability density of vertical velocity at five levels of a convective mixed layer. (After Caughey, et al., 1983; and Deardorff and Willis, 1985).

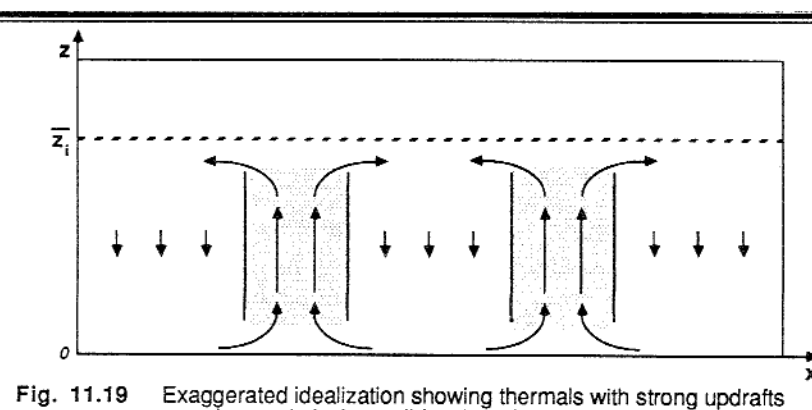

Fig. 11.19 Exaggerated idealization showing thermals with strong updrafts covering a relatively small fraction of the area, with weak downdrafts in between.

Although not plotted here, temperature histograms show negatively skewed frequency distributions in the ML, which change to symmetric distributions in the entrainment zone, similar to those of vertical velocity.

Joint probability distributions showing the relative frequency of vertical velocities and temperature fluctuations are shown in Fig 11.20 (Mahrt and Paumier, 1984; Deardorff and

Willis, 1985). In the bottom 2/3 of the ML (Fig 11.20b) there is a predominance of cool downdrafts. At the top of the ML, however, we see a peak associated with cool updrafts (Fig 11.20c). In fact, there is a broad peak associated with both updrafts and downdrafts that are cool. These are the tops of thermals overshooting into the entrainment zone and then sinking back down.

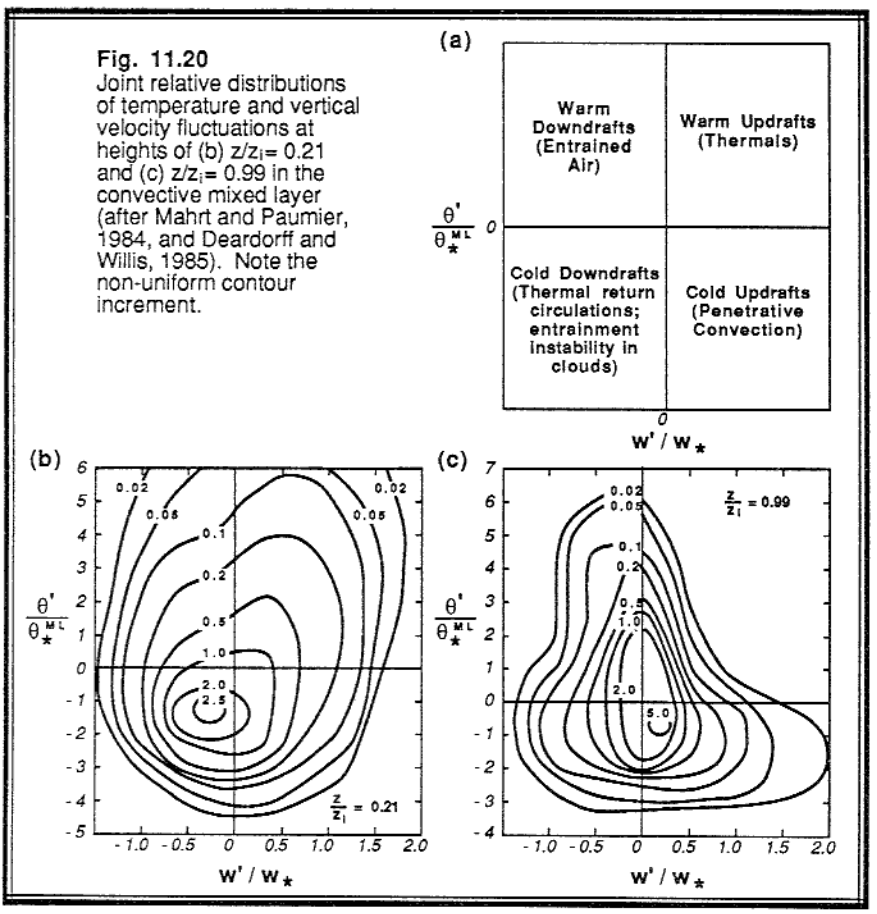

Fig. 11.20
Joint relative distributions of temperature and vertical velocity fluctuations at heights of (b) $z/z_i = 0.21$ and (c) $z/z_i = 0.99$ in the convective mixed layer (after Mahrt and Paumier, 1984, and Deardorff and Willis, 1985). Note the non-uniform contour increment.

Associated with the updrafts and downdrafts are corresponding horizontal convergence zones under thermals, and divergence above. The whole process is a circulation that moves air up and down in the mixed layer with a time period on the order of $t_* = z_i/w_*$, namely about 5 to 15 min.

When the tops of the thermals rise into the statically stable air of the entrainment zone, they become negatively buoyant. This causes a deceleration of the rising thermal, and eventually leads to its sinking back down into the mixed layer. This process is sometimes called penetrative convection (Scorer, 1957; Deardorff, et al., 1969, Stull, 1973).

Thermals are trapped within the mixed layer, which means that moisture and pollutants transported from the surface by thermals are also trapped.

The penetrative convection process and overshooting of thermals causes entrainment of large (horizontal and vertical thicknesses on the order of z_i) blobs or curtains of free atmosphere air down into the mixed layer between thermals, resulting in growth of the mixed layer thickness. Although portions of some of these entrained blobs have been observed to occasionally move down to the surface layer, most of the entrained air is mixed with surrounding ML air before reaching the surface. Using moisture as an indicator of source region of air, Crum and Stull (1987) found that undiluted surface layer air frequently reaches the top of the ML, presumedly in undiluted cores of thermals, while entrained FA air did not reach below 0.5 z_i for the cases studied (Fig. 11.21).

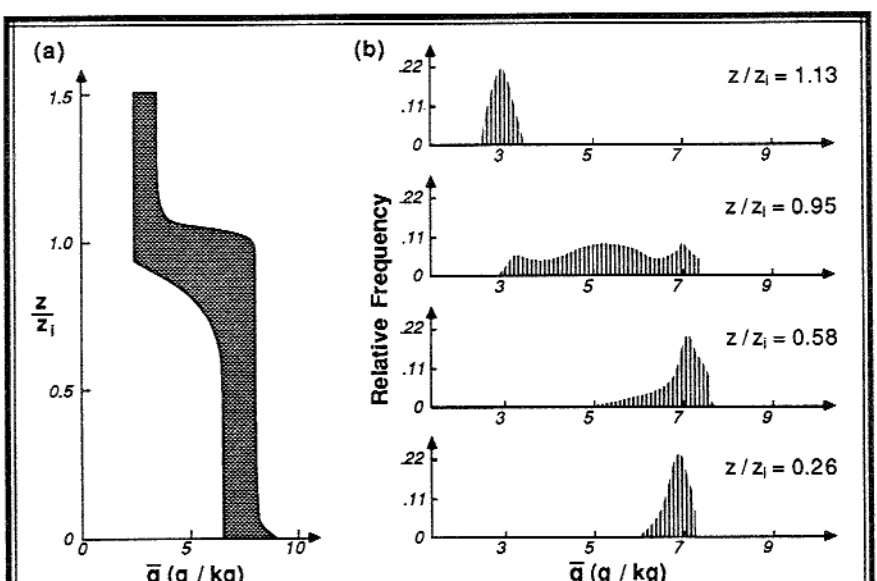

Fig. 11.21 Range of specific humidity measured by aircraft at various heights within the convective mixed layer during BLX83. (After Crum and Stull, 1987).

On a smaller scale, small eddies cause mixing into the top and sides of the thermal. Mixing into the top of individual thermals has been related to enhanced wind shear across the overshooting tops, resulting in the generation of turbulence via the Kelvin-Helmholtz process (Rayment and Readings, 1974). In spite of this process, little if any thermal air is mixed out of the thermal and deposited into the free atmosphere.

Lateral entrainment, or ***intromission***, appears to be a process where blobs of environmental air from outside the thermal are mixed horizontally into the thermal (Crum, et al., 1987). In the center of the thermal is a relatively undiluted core, carrying surface layer air up to the top of the boundary layer. Around this core is a thick contorted layer of

varying thickness in which some of the entrained environmental air and thermal air have mixed. Thus, there are no well defined edges to the typical thermal (Fig 11.22).

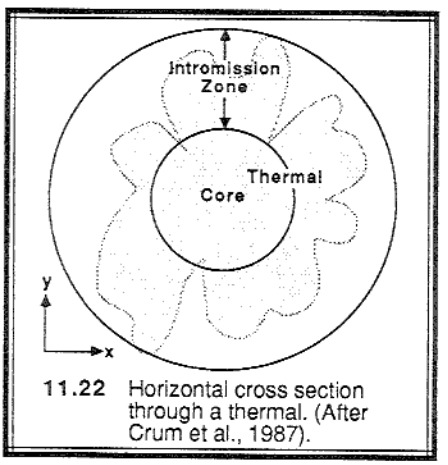

11.22 Horizontal cross section through a thermal. (After Crum et al., 1987).

This amorphous boundary between the updraft and downdraft region results in a variety of interpretations of convective structures as visualized using both *in-situ* and remote sensors. ***Conditional sampling*** is the technique of sorting data into thermal or non-thermal categories according to some selection criteria, called an ***indicator function***. The three most used indicators of thermals based on direct measurements are vertical velocity, humidity, and/or turbulence.

Usually, some minimum ***threshold amplitude*** of the indicator function must be met to determine the category of a data value. Within thermals, the fluctuations of these variables are sometimes greater than their respective conditionally sampled means. Thus, some sampling strategies also require that the indicator variable maintain a certain value over specified time ***durations*** (corresponding to a minimum size of the structure). Using both amplitude and duration, many data points can be sorted into the ***updraft (thermal) or downdraft categories***. Those remaining data points in the time series that satisfy neither the criteria for thermal updraft nor between-thermal downdraft are sometimes grouped into a third category called ***environment***.

Conditional sampling of aircraft data suggests that well-defined updrafts cover about 15 to 43% of the horizontal area, while well-defined downdrafts cover about 20 to 55% (Lenschow and Stephens, 1980, 1982; Greenhut and Khalsa, 1982, 1987; and Khalsa and Greenhut, 1985, 1987; Crum, et al., 1987; Young, 1988a-c). The remaining percentage are weaker circulations of mixed environmental air. Godowitch (1986) observed 36 to 40% updrafts and 49 to 52% downdrafts over both rural and urban sites, but thermals at the urban sites had greater vertical velocities.

Thermal diameters, as well as cumulus diameters, occur with a frequency that is approximately lognormally distributed. On some field experiments, a range of one to three thermal centers are encountered per horizontal flight distance of z_i. This suggests that

updrafts cluster, because the dominant wavelength of the vertical velocity spectra in MLs is at a wavelength of 1.5 z_i (Young, 1988)

Also, the number of well-defined thermal events decreases with height within the ML, suggesting that some of the thermals do not succeed in rising to the ML top. However, the diameter of thermals increases with height, suggesting that some thermals merge as they rise (Greenhut and Khalsa, 1987).

Conditionally sampled average values of vertical velocities and temperatures in updrafts and downdrafts are plotted in Fig 11.23. As expected, the virtual temperature excess in thermals is greatest at the ground, and can become negative at the top of the ML. Downdrafts at the ML top consist of warm entrained air, but lower in the ML the downdrafts are increasingly colder than the average ML temperature. The wide range of values indicated in this figure is related, in part, to differing definitions for indicator functions used by different investigators.

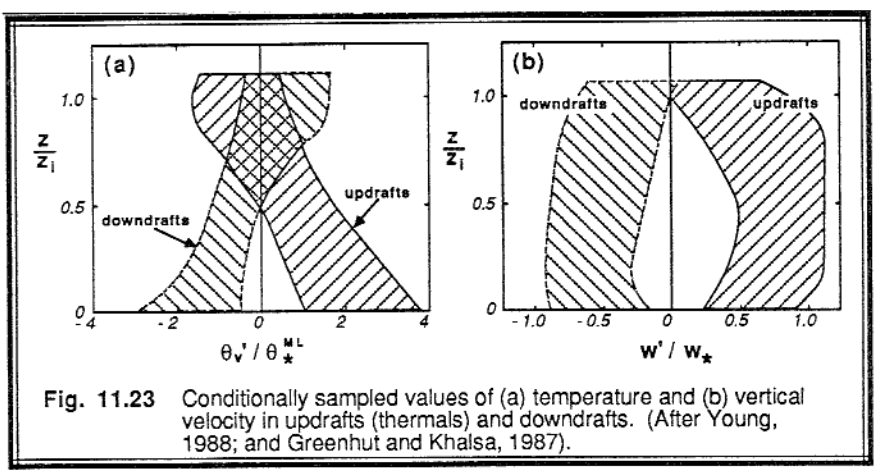

Fig. 11.23 Conditionally sampled values of (a) temperature and (b) vertical velocity in updrafts (thermals) and downdrafts. (After Young, 1988; and Greenhut and Khalsa, 1987).

Part of the difficulty in defining thermal boundaries is that although thermals start rising in the bottom third of the boundary layer as elements that are warmer than their environment, they are found to be cooler than their environment in the entrainment zone region. Some thermals gain most of the buoyancy from their moisture content, allowing the top half to be cooler than the environment even though the middle third might still be positively buoyant (using virtual potential temperature).

Lidar observations based on aerosol backscatter above some threshold (Hooper and Eloranta, 1986) tend to show the diameters of thermals decreasing with height (Fig 11.24), while Doppler sodar based on upward velocity above some threshold sometimes shows constant or increasing diameters (Taconet and Weill, 1983; Coulter, et al., 1985).

Almost all of the observations indicate that the thermals are not like bubbles, but are more like finite length columns that persist for some time. This suggests that the best model might be the "wurst" model — namely, the idealized thermal shape is like that of a sausage or wurst. Real thermals are not perfect columns of rising air, but twist and

meander horizontally and bifurcate and merge as they rise. Nevertheless, thermals are anisotropic, with most of their energy in the vertical.

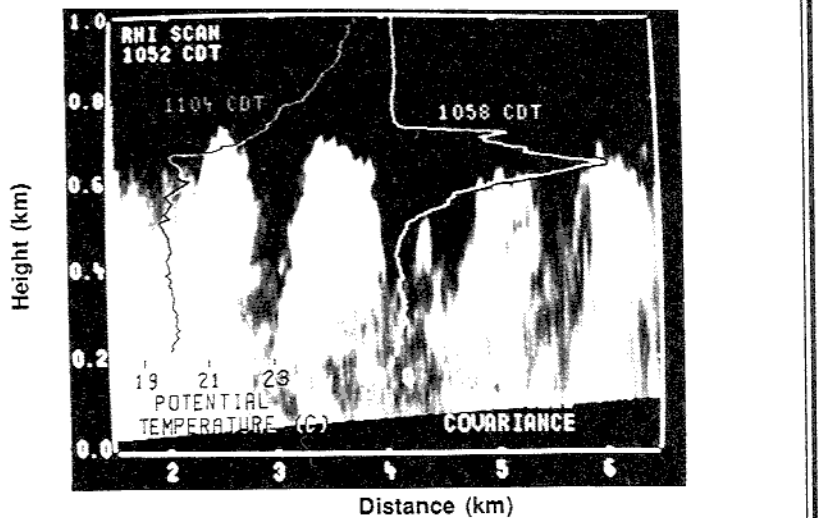

Fig. 11.24 RHI scan taken on 17 July at 1052 CDT. The light areas are areas of high aerosol concentrations carried aloft by rising convective plumes. The left overlay graph is the potential temperature profile at 1104 CDT. The right overlay is the normalized covariance profile of the aerosol density inhomogeneities. (After Hooper, 1982).

When hot spots exist on land surfaces, thermals predominantly form there (Smolarkiezicz and Clark, 1985). Glider pilots look for such hot spots as indicators of persistent lift (Reichmann, 1978). Over moist or vegetated surfaces, thermals are often moister than their environment. They are also usually more turbulent. Thermals are observed over oceans as well as land surfaces, suggesting that a surface hot spot is not necessarily needed as a triggering mechanism. In the absence of hot spots, thermals can be swept into lines or rings by weak mesoscale motions called ***secondary circulations***. These patterns are visible from satellite by the cloud streets and open/closed cells.

The "ultimate" hot spot was created in a classical field experiment in France (Bénech, et al., 1986; Noilhan, et al., 1986; Noilhan and Bénech, 1986) where an array of 105 oil burners generating a total heat output of 1000 MW distributed over 15000 m^2 of the surface were used to artificially create a convective thermal. Upwind of the warm updraft a cool downdraft was observed, while downwind a cool updraft was found. A pressure deficit of about 0.1 kPa (1 mb) was generated near the surface under the updraft, which induced horizontal convergence.

11.2.5 Horizontal Roll Vortices and Mesoscale Cellular Convection

During conditions of combined surface heating and strong winds, weak horizontal helical circulations can form in the boundary layer (Kuettner, 1959; Brown, 1970; LeMone, 1973, 1976; Kropfli and Kohn, 1978; Doviak and Berger, 1980; Mason and Sykes, 1980, 1982; Reinking, et al., 1981; Rabin and Doviak, 1982; Wilczak and Businger, 1983; Kelly, 1984; Atlas, et al., 1986). These circulations are called ***horizontal roll vortices*** or ***rolls***, and consist of clockwise and counterclockwise pairs of helices with their major axis aligned almost parallel with the mean wind. Some studies suggest that the roll axis should be roughly 18° to the left of the geostrophic wind direction for nearly neutral conditions, and that the angle decreases as the mixed layer becomes more statically unstable. The depth of these rolls equals the ML depth, and the ratio of lateral to vertical dimensions for a roll pair is about 3:1 (see Fig 11.25).

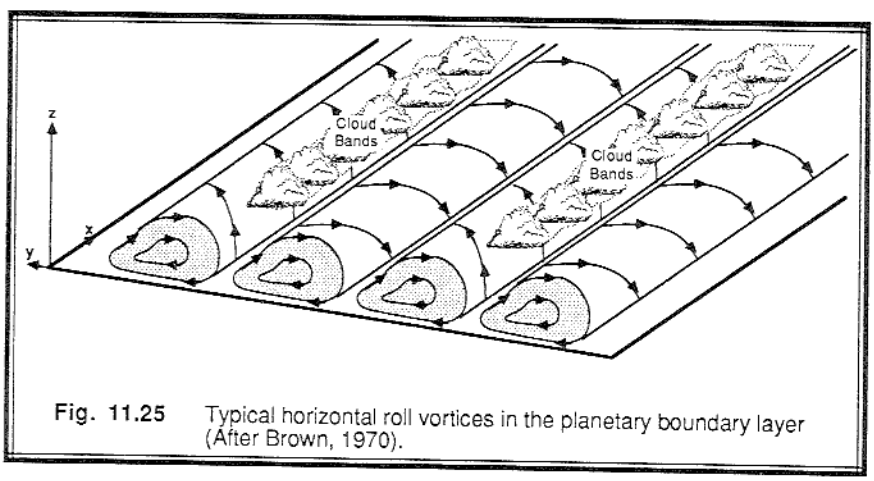

Fig. 11.25 Typical horizontal roll vortices in the planetary boundary layer (After Brown, 1970).

Tangential velocities around the helices are usually less than 1 m/s and are difficult to measure directly, although faster velocities occasionally occur. However, these velocities sweep other convective plumes and thermals into rows, creating along-wind rows of strong updraft. If sufficient moisture is present, ***cloud streets*** can form along these updraft rows. Such cloud streets are readily apparent from satellite imagery, particularly over ocean regions where there are no surface hot spots to destroy the organization.

Rolls are frequently observed during cold-air advection over warmer bodies of water, and are strongly associated with air-mass modification. Rolls are also common in the low-level jet ahead of cold fronts, and can occur between pairs of closed isobars of warm season anticyclones. Forest fires are also modulated by rolls, as is evident by long rows of unburned tree crowns in the middle of burned areas (Haines, 1982).

Theories for roll formation include thermal instabilities and inertial instabilities. Thermally, we would expect there to be less friction on the rising thermals if they align in rows, because thermals would have neighbors that are also updrafts. Thus, alignment into rows can be buoyantly more efficient, and the alignment provides protection from the

ambient wind shear. Other studies have suggested that secondary circulations such as rolls develop whenever an inflection point occurs in the mean wind profile. For example, the Ekman spiral solution always has an inflection point near the top of the Ekman layer.

Over the ocean, roll patterns and cloud streets gradually change to cellular patterns further downwind in a cold air advection situation. These are evident as honeycomb cloud patterns visible by satellite. This pattern is caused by ***mesoscale cellular convection*** (***MCC***, not to be confused with mesoscale convective complex). Open cells consists of hexagonal rings of updraft and clouds around clear central areas of downdraft, while closed cells are clear rings of descending air around mesoscale cloud clusters and updrafts. Cells typically have diameters on the order of 10 to 100 km, but are nevertheless boundary layer phenomena. Cells have depths on the order of 2 to 3 km, yielding aspect ratios of about 10:1 to 30:1 (Agee, et al., 1973; Rosmond, 1973; Lenschow and Agee, 1976; Sheu and Agee, 1977; Agee, 1984; Rothermel and Agee, 1980, 1986; Ray 1986).

The cellular pattern is reminiscent of laboratory ***Rayleigh-Bénard convection*** cells, except that the laboratory convection has an aspect ratio of about 1:1. These laboratory cells are well explained by the ***Rayleigh number***, Ra:

$$\mathrm{Ra} = \frac{g \Delta\bar{\theta}\, h^3}{\bar{\theta}\, \nu\, \nu_\theta} \qquad (11.2.5a)$$

for nonturbulent flow, where $\Delta\theta$ is the potential temperature difference across the convective layer of depth h, and where molecular viscosity, ν, and thermal diffusivity, ν_θ, dominate.

Many attempts have been made to define a ***turbulent Rayleigh number*** (using eddy diffusivities in place of the molecular ones) that would work for the atmosphere (Rothermel and Agee, 1986; Chang and Shirer, 1984; Fiedler, 1984). Although investigators have been able to numerically simulate some of the characteristics of MCC, they were often forced to make rather arbitrary choices for some of the model parameters. Frequently, the parameterization requires a rather large value of eddy diffusivity: in the range of 20 to 2000 $m^2 s^{-1}$. Ray (1986) has suggested that horizontal variability of K is necessary to explain MCC.

11.2.6 Dispersion

When pollutants are emitted at the bottom of the mixed layer they are quickly drawn by the convergence zones into the rising updraft, causing the center of mass of the tracer to initially move slightly above $0.5z_i$ as it drifts downwind (Fig 11.26a). Pollutants emitted above the surface layer move downward on the average (Fig 11.26b) because downdrafts comprise a larger area than updrafts, and because the updraft air is quickly recycled back down (Willis and Deardorff, 1976, 1978, 1981). Eventually, the pollutants become

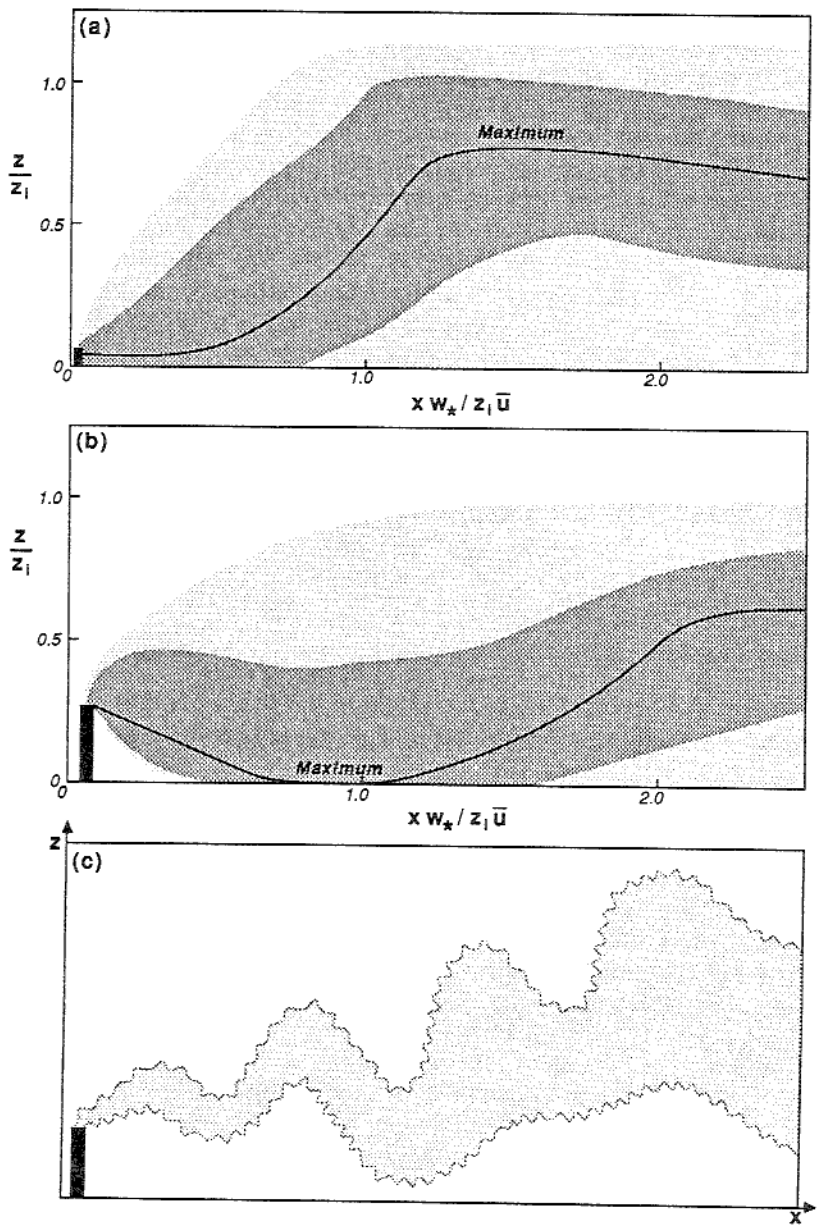

Fig. 11.26 Smoke plume behavior in a convective mixed layer: (a) time-averaged concentrations from a surface source; (b) same as (a) for an elevated source; (c) idealized snapshot of plume from an elevated source.

uniformly mixed in the vertical regardless of their source altitude, as expected in a well-mixed layer (Nieuwstadt and van Dop, 1982). This time-averaged statistical behavior should not be confused with the instantaneous ***looping*** of smoke plumes (Fig 11.26c).

Such dispersion within MLs has been observed during the Condors field program (Kaimal, et al., 1986). It has also been simulated with LES models (Deardorff, 1972; Lamb, 1978), and parameterized using asymmetric matrices in transilient turbulence theory (Stull, 1988).

As mentioned before, pollutants transported up from the surface by thermals are trapped beneath the capping inversion. Certain types of cumulus clouds (see Chapter 13) can break through the stable entrainment zone to ***vent*** pollutants and moisture out of the boundary layer into the free atmosphere.

11.2.7 Examples

Problem 1: Given a cloud-free ML with constant $w_e = 0.1$ m/s, and a constant divergence of $Div = 5 \times 10^{-5}\ s^{-1}$, find the ML depth versus time. The initial conditions are $z_i = 0$ at $t = t_o = 0$.

Solution: We can integrate the continuity equation from the surface up to z_i to find the subsidence velocity at the ML top:

$$w_L|_{z_i} = - Div \cdot z_i \qquad (11.2.7a)$$

When this is used in (11.2.2a), we get the prognostic equation:

$$\frac{dz_i}{dt} = w_e - Div \cdot z_i \qquad (11.2.7b)$$

Upon collecting terms, we can rewrite this equation as:

$$\frac{dz_i}{w_e - Div\, z_i} = dt$$

which can be easily integrated to yield:

$$z_i = \frac{w_e}{Div} - \left[\frac{w_e}{Div} - z_i(t_o) \right] \cdot e^{- Div \cdot (t - t_o)}$$

The resulting values for ML depth as a function of time are:

t (h):	0	1	2	3	4	5	10	20
z_i (m):	0	329	605	834	1026	1187	1669	1945

Discussion: We see that in a ML with constant divergence, the subsidence velocity increases with height, making ML growth more difficult. In fact, for our particular example, the ML top can not grow past 2 km, because at that height the subsidence is strong enough to completely counteract entrainment (Fig 11.27). As we will discover in section 11.4, the entrainment velocity also becomes smaller as the ML deepens. These two factors combine to limit the depth of the ML. Cases have been observed in the field where subsidence becomes so strong as to push the ML top downward, even while entrainment is happening.

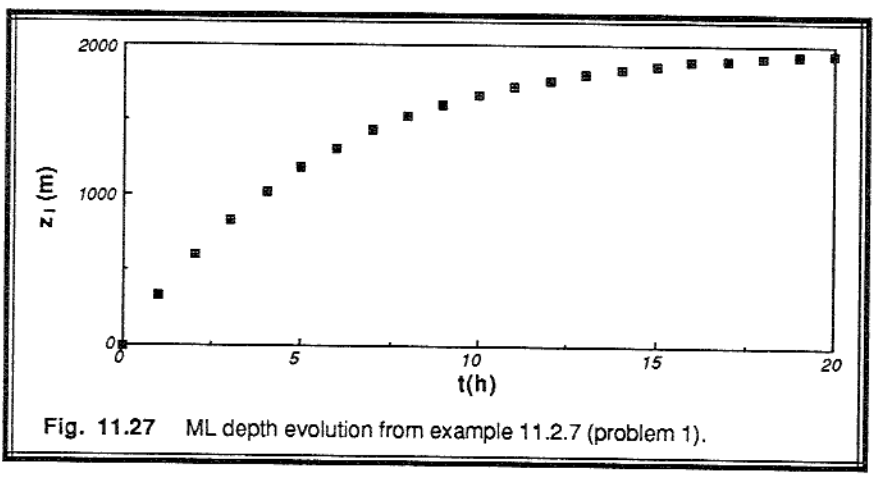

Fig. 11.27 ML depth evolution from example 11.2.7 (problem 1).

Problem 2: Suppose that the initial potential temperature sounding is $\theta = \theta_o + \gamma \cdot z$, where $\theta_o = 300$ K and $\gamma = 0.01$ K/m. Also assume that the surface heat flux is constant with time: $\overline{w'\theta'}_s = 0.2$ K m/s. If $z_i = 0$ at $t = 0$, use the thermodynamic method to find z_i and θ_{ML} at $t = 4$ h.

Solution: This problem can be represented graphically (see Fig 11.28). We wish to make the two shaded areas equal.

Heat Supplied = $(0.2 \text{ K m/s}) \cdot (4 \text{ h}) \cdot (3600 \text{ s/h}) = 2880 \text{ K} \cdot \text{m}$,

Heat Absorbed = $0.5 \cdot (\text{base}) \cdot (\text{height}) = 0.5 \cdot (\theta_{ML} - \theta_o) \cdot z_i = 0.5 \, \gamma \cdot z_i^2$.

Equating the two heats, we find that: $z_i = [2\cdot(2880)/0.01]^{1/2} = 758.9$ m. The ML potential temperature is $\theta_{ML} = \theta_o + \gamma\cdot z_i = 300 + (0.01)\cdot(758.9) = 307.6$ K.

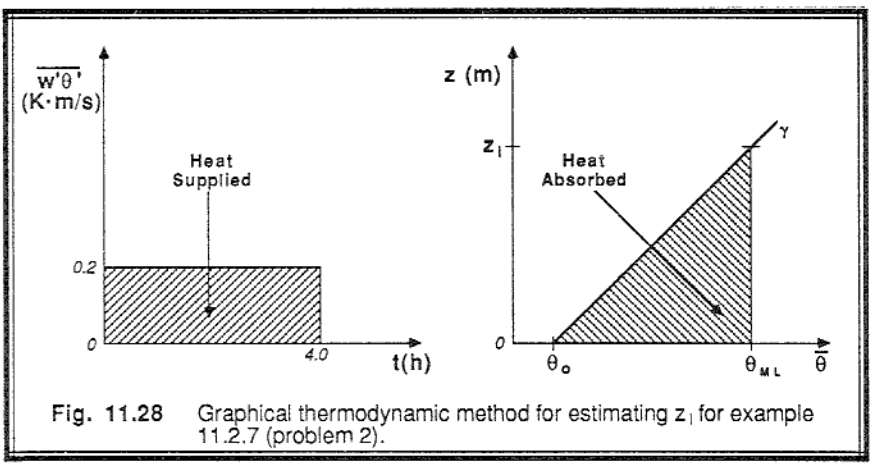

Fig. 11.28 Graphical thermodynamic method for estimating z_i for example 11.2.7 (problem 2).

Discussion: In reality, the heat flux usually varies with time, and the initial sounding is much more complex, making the solution more difficult, but not impossible.

11.3 The Entrainment Zone

11.3.1 Characteristics

The entrainment zone (EZ) is the region of statically stable air at the top of the ML, where there is entrainment of FA air downward and overshooting thermals upward. The EZ can be quite thick — averaging about 40% of the depth of the ML.

The top of the entrainment zone is defined as the altitude, h_2, of the top of the highest thermal within a region. The bottom, h_o, is more difficult to define because there is no sharp demarcation. The bottom is usually taken as that altitude where about 5 to 10 % (Deardorff, et al., 1980; Wilde, et al., 1985) of the air on a horizontal plane has FA characteristics (Fig 11.29a). An alternative definition of the EZ is that region where the buoyancy flux, $\overline{w'\theta_v'}$, is negative (see Fig 11.1). The entrainment zone is quite apparent and easily measurable using remote sensors such as lidar (Boers, et al., 1984; Crum and Stull, 1987).

The altitude of the ***local ML top***, shown by the solid line in Fig 11.29a, varies significantly between the EZ top and the middle of the ML. Its shape looks like a series of inverted "U"s marking the tops of penetrating thermals. The ***average ML depth,*** which we traditionally call z_i, is the altitude where 50% of the air has FA characteristics on a horizontal average. Thus, z_i is just below the midpoint between h_2 and h_o.

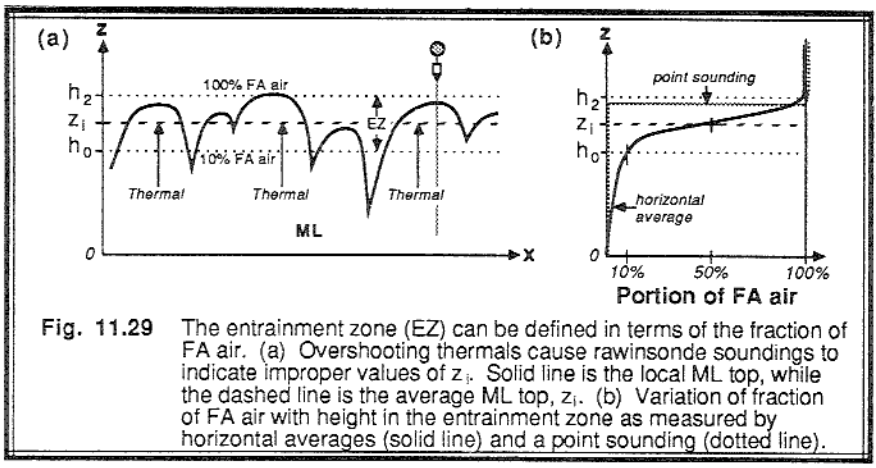

Fig. 11.29 The entrainment zone (EZ) can be defined in terms of the fraction of FA air. (a) Overshooting thermals cause rawinsonde soundings to indicate improper values of z_i. Solid line is the local ML top, while the dashed line is the average ML top, z_i. (b) Variation of fraction of FA air with height in the entrainment zone as measured by horizontal averages (solid line) and a point sounding (dotted line).

When horizontal averages of temperature or moisture are taken by aircraft in the EZ, the resulting profile of percentage of FA air vs height exhibits a smooth profile (Fig 11.29b). However, a rawinsonde sounding made through a single point will likely show a sharp jump (Mahrt, 1979) in temperature, moisture and wind (Fig 11.29b) when it encounters the local ML top. Since this local top can be at a significantly different altitude than the average top depending on which location is penetrated by the sensor, we recommend that single rawinsonde soundings NOT be used to estimate z_i. Rawinsonde z_i errors can easily be as large as 0.4 z_i.

11.3.2 Evolution and Models

When the ML is shallow in the morning over land, the EZ is proportionally shallow. As the ML grows, so does the EZ thickness (see Fig 11.10). Thin EZs are expected for large temperature changes across the ML top, because thermals will not penetrate as far and entrainment will be slow. Thick EZs are expected with more intense ML turbulence where convection is vigorous.

Deardorff, et al. (1980) have suggested that the ratio of EZ thickness (Δh) to depth of the ML (using h_o as one measure), is:

$$\frac{\Delta h}{h_o} = 0.21 + 1.31\,(Ri^*)^{-1} \qquad (11.3.2a)$$

where Ri^* is a ***convective Richardson number***, defined by:

$$Ri^* = \frac{g\,\Delta_{EZ}\bar{\theta}_v\,z_i}{\bar{\theta}_v\,w_*^2} \qquad (11.3.2b)$$

The -1 power law dependence is still debated in the literature, with other suggestions ranging from 0 to -2.

In the evening over land, when ML turbulence decays, we are left with the statically stable ***capping inversion*** in place of the EZ. In fact, the EZ is often called the capping inversion during the day because it acts as a lid to convection. In the absence of turbulence, there is little change to the capping inversion at night, except by subsidence and advection.

We can also model the distribution of FA air within the EZ. As mentioned before, the amount of FA air decreases with distance down from the top of the EZ. Also present in the EZ are some thermal cores that have transported up rather undiluted surface layer (SL) air. Smaller eddies mixing these two extremes creates a third category of air that we will call mixture air.

The relative fractions of these three air categories is plotted in Fig 11.30 based on the tank measurements of Deardorff, et al. (1980) and the aircraft field observations of Crum, et al. (1987). Sometimes mixture air and SL air are grouped together and called mixed layer air (Deardorff, et al., 1980). Wilde, et al. (1985) found that the distribution of ML air with height is fairly-well described by the integral of a truncated double-exponential function, with the peak centered at z_i.

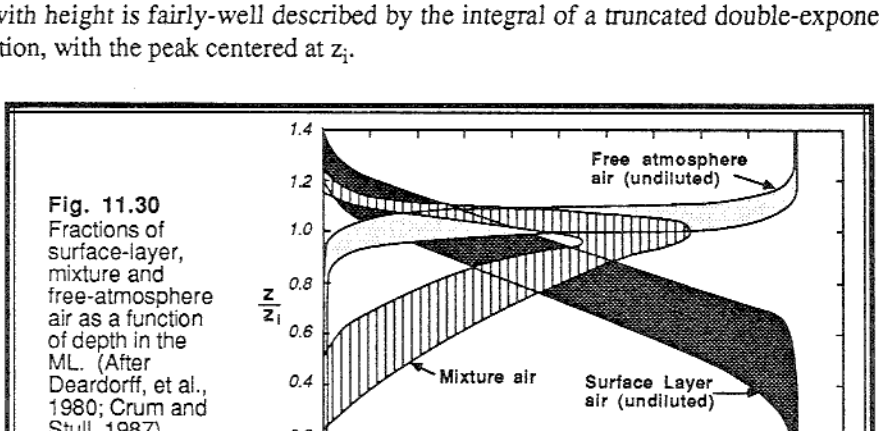

Fig. 11.30 Fractions of surface-layer, mixture and free-atmosphere air as a function of depth in the ML. (After Deardorff, et al., 1980; Crum and Stull, 1987).

11.3.3 Structures

Overshooting and Intermittancy. The entrainment zone essentially consists of turbulent thermals imbedded within non-turbulent FA air. An aircraft flying a horizontal flight leg within the entrainment zone will experience intermittent periods of turbulence.

A variety of smaller scales of motion are present in the entrainment zone in addition to the large overshooting thermals (Crum and Stull, 1987). In spite of this smaller-scale turbulence, there is very little (almost negligible) ML air dispersed out of the thermals into the FA.

K-H Waves. Kelvin-Helmholtz (K-H) waves can also exist on a variety of scales in the entrainment zone. On the largest scale, we recognize that there is wind shear between the sub-geostrophic ML air and the nearly geostrophic FA air. This shear across the statically stable entrainment zone is ideal for the formation of K-H waves, as discussed in Chapter 5. The waves formed in this manner often have a wavelength proportional to the depth of the EZ (i.e., hundreds of meters), and evolve rather slowly. They break, become turbulent, and can contribute to the entrainment of FA air into the ML.

On a smaller scale, K-H waves can form along the top boundary of overshooting thermals (Fig 11.31, after Rayment and Readings, 1974). The thermals are carrying up the cooler and slower ML air, and their tops are marked by a sharp interface with the FA air. As a result, there can be very strong shears and statically stable lapse rates across a distance of two to ten meters. This situation is ideal for the formation of short-wavelength, rapidly evolving K-H waves that form, break, and decay into turbulence during the few minutes that the thermal is penetrating into the EZ. The thin layer of turbulence that results along the top helps dilute the thermal, but contributes little to the overall entrainment into the ML.

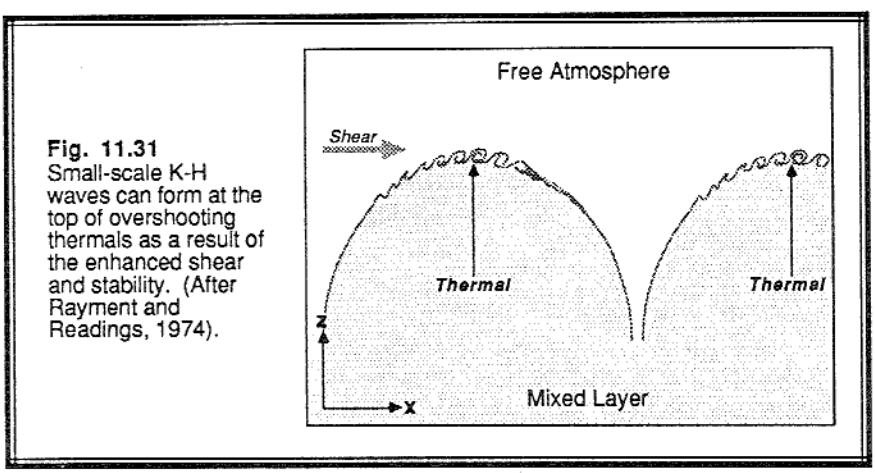

Fig. 11.31 Small-scale K-H waves can form at the top of overshooting thermals as a result of the enhanced shear and stability. (After Rayment and Readings, 1974).

Gravity Waves and Resonance with Convection. When thermals penetrate into the statically stable EZ and FA, ***internal gravity (buoyancy) waves*** can be excited in the FA (Fig 11.32a). These waves have been observed in laboratory tanks (Deardorff, et al., 1969) and simulated numerically (Deardorff, 1974; Carruthers and Moeng, 1987) with LES models. Depending on the static stability, these waves may propagate vertically and horizontally away from the thermals, and thus drain kinetic energy and momentum from those thermals (Deardorff, 1969). However, it appears that the portion of ML energy drained by internal waves is relatively small, and can usually be neglected (Stull, 1976).

Penetrating thermals and associated clouds are often moving at a different speed (usually slower) than the air aloft. As a result, the cloud acts like an obstruction to the

flow, and forces air to flow over its top, analogous to air flow over a mountain (Fig 11.32b). The result can be the same; namely, mountain-type waves can be generated. Such waves have be used by glider pilots, who have named them ***thermal waves or convection waves*** (Clarke, et al., 1986; Kuettner, et al., 1987). These convection waves have a horizontal wavelength of 5 to 15 km, a vertical motion amplitude of 1 to 4 m/s, and can extend upwards throughout the troposphere if the static stability is favorable. A 90° direction change in the wind shear vector near z_i supports thermal wave generation. Climatologically, thermals waves are often found in pre- and postfrontal zones, and the waves are often stronger over cloud streets than over isolated cumulus.

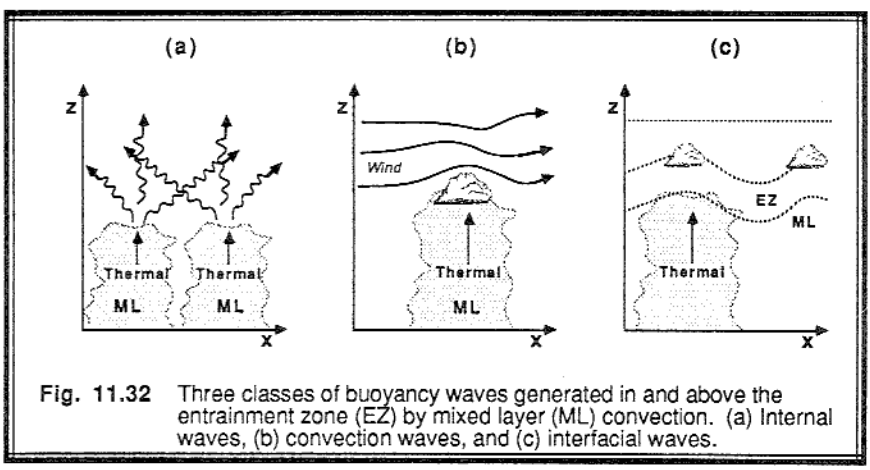

Fig. 11.32 Three classes of buoyancy waves generated in and above the entrainment zone (EZ) by mixed layer (ML) convection. (a) Internal waves, (b) convection waves, and (c) interfacial waves.

A third type of wave is an interfacial wave formed on (or trapped within) the EZ (Fig 11.32c). These are analogous to the surface waves excited when a pebble is tossed into a pond, and do not require a mean wind or wind shear in order to form. Wavelengths of the diameter of thermals and smaller experience very strong nonlinear interaction with ML turbulence, and are quickly absorbed into the ML (Weinstock, 1987). Longer wavelengths, however, can persist and modulate the organization of convection within the ML. As a result, resonance can occur where ML convection and clouds are enhanced at the same wavelength as the waves (Clark, et al., 1986; Noilhan, et al., 1986).

11.4 Entrainment Velocity and Its Parameterization

11.4.1 Typical Values

There are obvious bounds on the entrainment velocity based on the observed rise of the ML top. By definition, it can never be negative. If there is entrainment happening in both directions across a stable interface, then we can use separate (positive) velocities for the entrainment in each direction. It can be zero whenever there is no turbulence. Large values on the order of w_e = 1 m/s are possible during the rapid-rise phase of the late

morning ML, when the ML turbulence is strong and the capping inversion is weak. Typical values, however, are often in the range of $w_e = 0.01$ to 0.20 m/s.

As mentioned earlier, we must make an assumption to close the ML equations. This assumption can be in the form of a parameterization for the entrainment velocity, or a parameterization for any of the other unknowns in the set of equations (11.2.3a-d). Obviously, if assumptions are made for the other unknowns, then the entrainment velocity can be calculated from the other knowns. The following sections describe some of these closure assumptions. The thermodynamic method (Section 11.2.2) is not described here because it is a direct calculation of ML depth, without really using entrainment velocities. Of course, the thermodynamic methods works only during free convection, and fails whenever mechanical generation of turbulence dominates.

11.4.2 Flux-Ratio Method

For the case of free convection, the turbulence causing entrainment is directly related to the buoyancy flux at the surface. This causes the buoyancy flux at the top of the ML to be a nearly constant fraction of the flux at the bottom (Ball, 1960):

$$\frac{\overline{-w'\theta_v'}_{z_i}}{\overline{w'\theta_v'}_s} = A_R \qquad (11.4.2a)$$

Most of the suggested values of A_R range between 0.1 to 0.3, with $A_R = 0.2$ being a good average to use for free convection (Stull, 1976a). When humidities are low such that potential temperature and virtual potential temperature are approximately equal, (11.4.2a) is often written in terms of the heat flux.

When (11.4.2a) is used in an expression analogous to (11.2.3c) but for virtual potential temperature, we find that the entrainment velocity is:

$$w_e = \frac{A_R \overline{w'\theta'}_{v_s}}{\Delta_{EZ}\bar{\theta}_v} \qquad (11.4.2b)$$

Almost all of the entrainment parameterizations have this same fundamental form: entrainment is proportional to some measure of the turbulence or external turbulence forcing, and is inversely proportional to the virtual potential temperature jump across the top of the ML. Stronger capping inversions reduce entrainment, while stronger surface buoyancy flux increases entrainment.

11.4.3 Energetics Method

In situations where wind shear generates turbulence, the previous method fails. Quite a few alternative parameterizations have been proposed in the literature that include mechanical as well as thermal generation of turbulence. One class of entrainment closure, described here, uses the TKE equation.

In order for warm air to be entrained into the cooler ML, it must be forced down against the restoring force of gravity. In the process of lowering the buoyant entrained air, the potential energy of the ML/FA system is increased. The rate of change of potential energy with time equals the integral over height of the negative portions of buoyancy flux. Some of the TKE of the ML is expended to do the work necessary to bring the entrained air down. The net result is that some TKE has been converted to potential energy.

To get an entrainment velocity from this approach, start by integrating the TKE equation (5.1) over the total depth of the boundary layer (Stull, 1976a):

$$\frac{d}{dt}\int \bar{e}\, dz = \frac{g}{\bar{\theta}_v}\int \overline{w'\theta_v'}\, dz - \int \overline{u'w'}\frac{\partial \bar{U}}{\partial z}\, dz - \frac{1}{\bar{\rho}}\overline{w'p'}_{z_i} - \int \varepsilon\, dz \qquad (11.4.3a)$$

$$\text{St} \qquad B_{PN} \qquad \text{MP} \qquad \text{GW} \qquad \text{Dis}$$

where St is the integrated storage term, B_{PN} is buoyancy, MP is the mechanical production, GW is a pressure-velocity correlation related to gravity waves draining energy from the top of the ML, and Dis is viscous dissipation. Note that the turbulent transport term (Term V in equation 5.1b) integrates to zero and does not appear above because there is no turbulent transport into the nonturbulent FA or into the ground. As mentioned before, the GW term is relatively small, and can usually be neglected.

Suppose that the buoyancy flux at any height can be split into positive and negative contributions, identified as production and consumption respectively (Stage and Businger, 1981):

$$\overline{w'\theta_v'} = \overline{w'\theta_v'}\Big|_{\text{production}} + \overline{w'\theta_v'}\Big|_{\text{consumption}}$$

The integral of buoyancy flux in term B_{PN} could thus be split into two parts, $B_{PN} = B_P + B_N$:

$$B_p = \frac{g}{\bar{\theta}_v}\int \overline{w'\theta_v'}\Big|_{\text{production}} dz \qquad \text{and} \qquad B_N = \frac{g}{\bar{\theta}_v}\int \overline{w'\theta_v'}\Big|_{\text{consumption}} dz \qquad (11.4.3b)$$

where B_P represents the ***production*** of TKE via buoyancy, and B_N represents the ***consumption*** of TKE as it is converted into potential energy. Although B_P and B_N

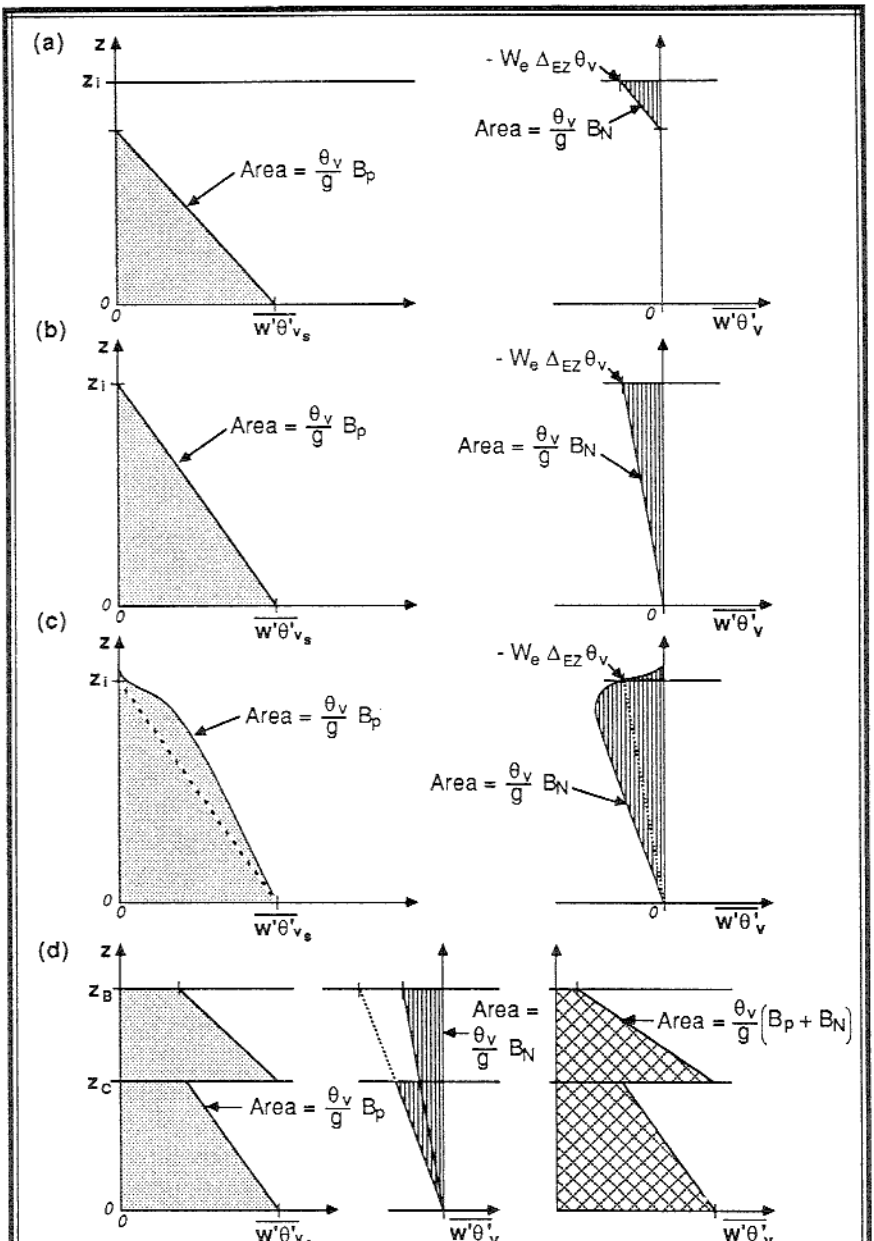

Fig. 11.33 Different models for production, B_P, and consumption, B_N, of TKE in the ML. The sum of the two curves in (a) equals the total heat flux, as plotted in Fig. 11.13. The curves in (b) and (c) also sum to the same total. Fig. (d) show the corresponding curves for an idealized stratocumulus-topped ML. (After Stage and Businger, 1981).

appear to have the same definition, only the subset of buoyancy flux that is negative is used in B_N, and the remainder is used in B_p.

The critical question is how to partition the buoyancy flux profile into its production and consumption components. One way is to focus on just the positive and negative portions of the total buoyancy flux profile (Fig 11.33a). Randall (1984) has called this the ***Eulerian partitioning*** approach. Alternative geometries have also been suggested (Fig 11.33b&c) based on ***process partitioning*** of updrafts vs. downdrafts (Randall, 1984), and some parameterizations can be used for cloud topped MLs (Fig 11.33d). The correct answer has yet to be pinned down, but luckily most partitioning schemes yield similar answers for the entrainment velocity.

To close this equation and solve for entrainment velocity, we must make a few additional assumptions or parameterizations. Quasi-steady state is often assumed, allowing us to set St = 0. The integrated TKE equation now becomes:

$$-B_N = B_p - MP - Dis \qquad (11.4.3c)$$

where MP and B_N are usually negative. The buoyant production term, B_p, is known from the partitioning described above, and is equal to $(g/\overline{\theta_v})$ times the "production area" as sketched in Fig 11.33. When clouds are present, this production area should include the effects of radiation divergence (Stage and Businger, 1981). The mechanical production term, -MP, is often parameterized in terms of forcings, such as the shear or u_* at the surface and the shear ΔU across the top of the ML. The dissipation rate, Dis, is often assumed to be proportional to the total production rate (B_p - MP). Between 80% to 99% of the TKE produced is dissipated (Stull, 1976; Stage and Businger, 1981). At this point, we know all of the terms on the right of (11.4.3c), and can solve for the value of B_N.

Knowing B_N, the "consumption area" of the buoyancy flux profile (Fig 11.33) can be found from: consumption area = $B_N / (g/\overline{\theta_v})$. Using the geometry assumed earlier in the partitioning scheme, the consumption area can be related to the buoyancy flux at the top of the ML: $\overline{w'\theta_v'}_{z_i}$. The entrainment velocity can then be found from the relationship between temperature jump and entrained heat flux:

$$w_e = \frac{-\overline{w'\theta_v'}_{z_i}}{\Delta_{EZ}\overline{\theta_v}} \qquad (11.4.3d)$$

The advantage of this production/consumption approach is that it can be applied to a variety of situations: free convection, forced convection, mixed convection, and cloud-topped MLs.

As an example, when the energetics method is applied to a cloud-free ML with shear at both the surface and at the top of the ML, the following relationship can be derived (Stull, 1976a) assuming an Eulerian partitioning geometry as sketched in Fig 11.33a:

$$w_e = \frac{2\,\overline{\theta}_v}{g\,d_1\,\Delta_{EZ}\overline{\theta}_v}\left[\, c_1 w_*^3 + c_2 u_*^3 + c_3(\Delta_{EZ}\overline{U})^3 \,\right] \qquad (11.4.3e)$$

where the three parameters are $c_1 = 0.0167$, $c_2 = 0.5$, and $c_3 = 0.0006$. The first term in square brackets parameterizes buoyant production, the second surface mechanical production, and the last mechanical production at the top of the ML. The distance, d_1, is the distance between the top of the ML and the height where the heat flux profile crosses zero:

$$\frac{d_1}{z_i} = \frac{-\overline{w'\theta_v'}_{z_i}}{-\overline{w'\theta_v'}_{z_i} + \overline{w'\theta_v'}_s}$$

It can easily be shown that this energetics parameterization reduces to the flux-ratio parameterization for the special case of free convection.

11.4.4 Other Methods

There are many other methods that have appeared in the literature, and which won't be listed here. Most are variations of the above methods. Some, such as proposed by Deardorff (1979), offer generalized approaches that do not depend on a jump or slab type of model. Most approaches have been tested against observed data and give realistic results within the uncertainties of the data. Contributing to some of the uncertainty is subsidence, which is not easily measurable and can be as large as the entrainment velocity. Section 11.5 examines some of the characteristics of boundary layer subsidence.

There were some additional methods to forecast ML depth that were tested, but which did not work well. One method assumed that the ML depth was proportional to the Ekman layer depth. Another assumed that a bulk Richardson number could be formed using the wind and temperature difference across the whole ML depth, and that z_i was found using the requirement that the bulk Richardson number equal some constant critical value.

11.4.5 Example

Problem: Given: $\overline{w'\theta_v'} = 0.2$ K m/s, $u_* = 0.2$ m/s, $g/\overline{\theta_v} = 0.0333$ m s^{-2} K^{-1}, $z_i = 1$ km, $\Delta_{EZ}\overline{\theta_v} = 2$ K. Find w_e using the:

a) Flux ratio method; b) Energetics method (special case equation 11.4.3e).

Solution:
a) Flux ratio method:

$$w_e = A_R \frac{\overline{w'\theta_{v\,s}'}}{\Delta_{EZ}\overline{\theta_v}} = \frac{0.2 \cdot 0.2}{2} = 0.0200 \text{ m/s}$$

b) Energetics method:

$$w_e = \frac{2}{(g/\overline{\theta_v})\, d_1\, \Delta_{EZ}\overline{\theta_v}} \left[c_1 w_*^3 + c_2 u_*^3 \right] = \frac{30.03}{d_1} \left[0.1112 + 0.004 \right] = \frac{3.46}{d_1}$$

But

$$d_1 = 1000 \left[\frac{2 w_e}{0.2 + 2 w_e} \right]$$

Combining these two equations gives:

$$w_e^2 = 0.00173 \left[2 w_e + 0.2 \right]$$

which can be solved to yield $w_e = 0.0204$ m/s.

Discussion: We see that the addition of small values of surface stress have little effect on the entrainment rate in a free convection situation, and that the flux ratio method gives essentially the same answer with much fewer computations. For forced convection, however, the flux ratio method fails completely, but the energetics method can be used in the form (neglecting shear at the ML top, and using $d_1 = z_i$):

$$w_e = \frac{2\, c_2\, u_*^3}{(g/\overline{\theta_v})\, z_i\, \Delta_{EZ}\overline{\theta_v}}$$

11.5 Subsidence and Advection

11.5.1 Advection

Even with the large vertical fluxes and vigorous turbulence in a convective ML, horizontal advection of state characteristics by the mean wind can have as large an effect as turbulence. The equations of Chapters 3 to 5 include the mean advection terms, and will not be discussed in more detail here. Neglect of advection is unwarranted for most simulations of real boundary layer.

One measure of the relative importance of turbulence vs. the mean wind is the dimensionless convective distance, X^{ML} (Willis and Deardorff, 1976):

$$X^{ML} = \frac{x\ w_*}{z_i\ \overline{M}} \qquad (11.5.1a)$$

This can be interpreted as the ratio of measured horizontal distance to the theoretical distance traveled during one convective circulation (updraft and downdraft). For large X^{ML} (>>1) turbulent mixing dominates over the mean wind, while for small X^{ML} (<<1) the turbulent mixing is less important.

In addition to horizontal advection of momentum, moisture, heat, and pollutants, we must be concerned about advection of z_i. In essence, the latter is a measure of the advection of volume within the ML. For example, a slowly rising, shallow ML over a moist irrigated region can grow rapidly if a deeper ML advects into the area. The local change of z_i is described by:

$$\frac{\partial z_i}{\partial t} = -U_j \frac{\partial z_i}{\partial x_j} + w_e + w_L \qquad (11.5.1b)$$

The slope of z_i can be significant, and its neglect can cause forecast errors in ML depth tendency as great the magnitude of the entrainment velocity (Lenschow, 1973).

For strong winds and abrupt changes in surface conditions, advection can dominate to prevent growth of the local ML with time. The resulting thermal internal boundary layer, which is a function of downwind distance x, is discussed in Chapter 14.

11.5.2 Subsidence and Divergence

Mean vertical velocities ranging from -0.22 m/s (subsidence) to 0.27 m/s (upward motion) have been observed in a limited case study based on BLX83 field experiment data (Vachalek, et al., 1988). These magnitudes are very large compared to the entrainment velocity, and can not be neglected.

Unfortunately, subsidence at the top of the ML is very difficult to measure. Vertical velocity measurements from aircraft often have a mean bias that is greater than the true subsidence, and therefore cannot be used. The mean vertical velocity magnitudes are also below the noise level of most Doppler remote sensors. The downward movement of elevated smoke, moisture, or stable layers can be tracked, but usually horizontal advection affects this movement and is frequently not known. Also, the tracking of elevated layers can be applied only if the layers are in the FA above the mixed layer, so as not to be influenced by ML growth.

Alternately, mean vertical motion at z_i can be estimated if divergence is known as a function of height within the ML, using:

$$w_L(z_i) = -\int_{z=0}^{z_i} \mathrm{Div}(z)\, dz \qquad (11.5.2a)$$

For the special case of constant divergence with height, (11.5.2a) reduces to

$$w_L(z_i) = -\mathrm{Div} \cdot z_i \qquad (11.5.2b)$$

This latter expression is frequently used due to lack of better divergence data.

Horizontal divergence is not trivial to measure. Theoretically, we must measure the normal velocities out of a specified horizontal area, and we must make these measurements at every point on the perimeter of the area. Some remote sensors, such as Doppler radar and Doppler lidar, come closest to satisfying this requirement by measuring radial velocity at any specified range as a function of azimuth. A plot of this data is called a ***velocity-azimuth display (VAD)***. Unfortunately, ground clutter for the radar can contaminate the velocity statistics.

Surface mesonetwork stations placed close together along the perimeter of the area can be used to estimate divergence near the surface, assuming that surface terrain features do not contaminate the velocities. As stations are spaced further apart along the perimeter, divergence accuracy drops. If the diameter of the network is too small, then the horizontal velocity difference across the network could be too small to resolve.

Finally, a network of rawinsonde launch sites can be used to find divergence using the ***Bellamy method***; however, sonde accuracy, large site separations, and sonde-to-sonde calibration errors can contaminate divergence calculations. Vachalek, et al. (1988) found that the rawinsonde divergence integrated over the ML depth, and surface divergence from mesonetwork stations yielded the best results.

Divergence fluctuations on a wide range of horizontal and temporal scales are usually superimposed on each other. Smaller diameter features appear to have greater magnitudes (by factors of up to 100) and shorter durations than the large diameter features. For example, a region of diameter 5 km was found to have peak divergence magnitudes in the range of 10^{-4} to 10^{-5} s^{-1}, while regions of diameter 100 km had peak divergences of 10^{-5} to 10^{-7}. A comparison of the relative frequency of events of different divergence magnitude and horizontal scale is presented in Fig 11.34.

The short duration (1 h) divergence events occur about 10 times more frequently than long duration events, and about 95% of all divergence events had durations shorter than 8 h. This implies that divergence and subsidence estimated from a large-diameter network will not show large-magnitude short-period variations, and thus may be useless for estimating subsidence over a fixed point at any specific time.

Vachalek, et al. (1988) studied how the divergence variations were associated with meso- and synoptic-scale features, and developed the following idealized divergence models:

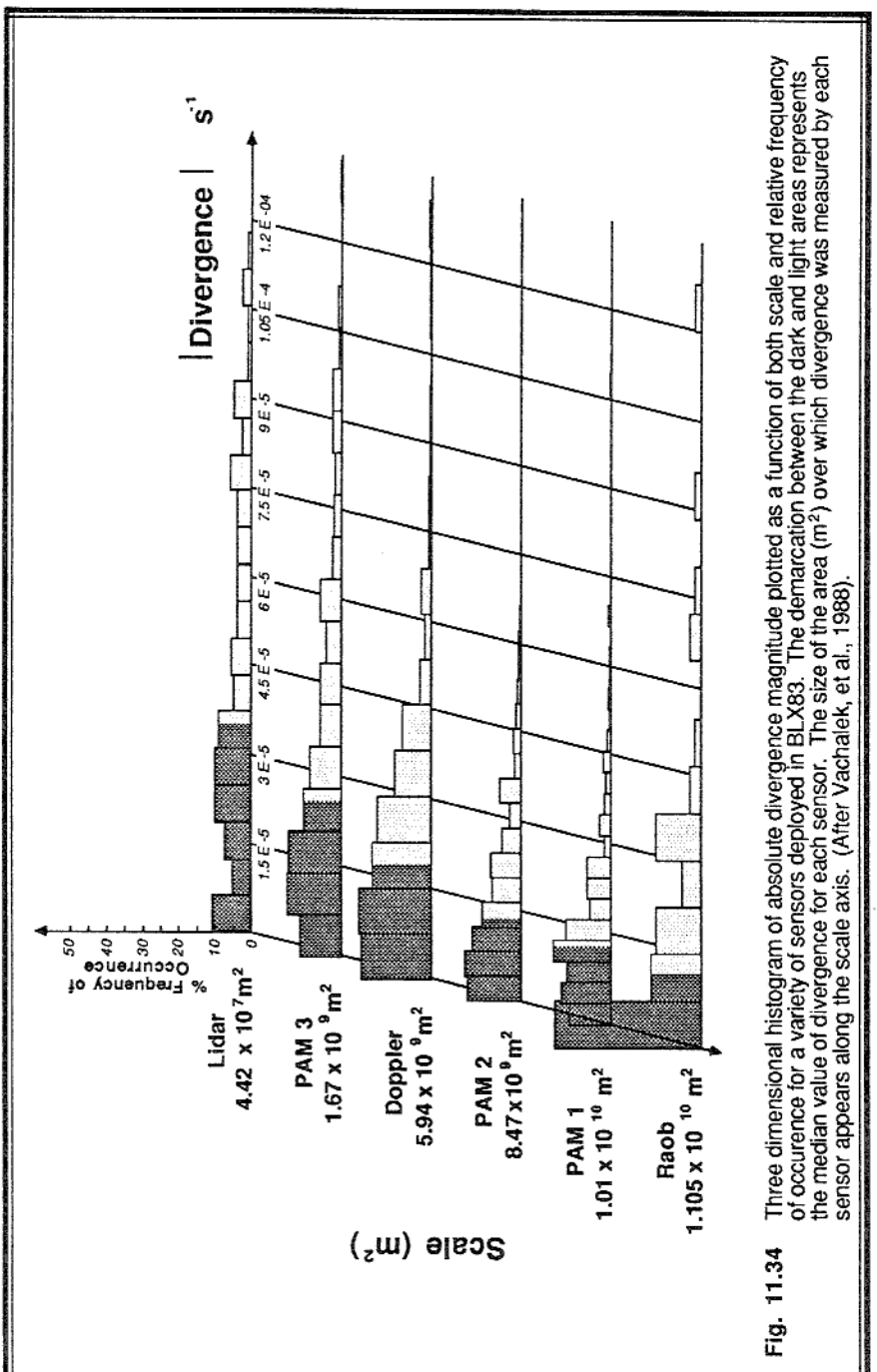

Fig. 11.34 Three dimensional histogram of absolute divergence magnitude plotted as a function of both scale and relative frequency of occurence for a variety of sensors deployed in BLX83. The demarcation between the dark and light areas represents the median value of divergence for each sensor. The size of the area (m^2) over which divergence was measured by each sensor appears along the scale axis. (After Vachalek, et al., 1988).

(1) 2-D divergence from high (convergence into low) pressure centers,
(2) 1-D divergence from ridges (convergence into troughs),
(3) 1-D step-like changes in velocity normal to fronts, associated with very large convergence across a very small zone, and
(4) convergence/divergence couplets associated with thunderstorm passage.

These models are sketched in Fig 11.35.

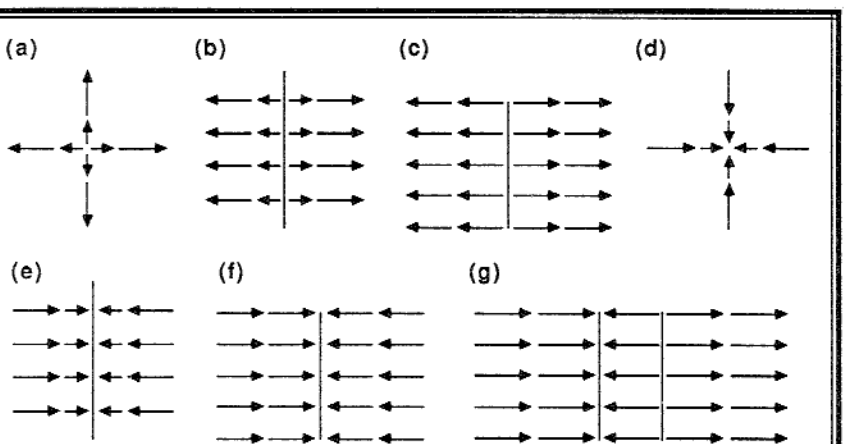

Fig. 11.35 Idealized models of (a) 2-dimensional divergence in a high pressure system, (b) 1-dimensional high pressure ridge-axis divergence, (c) step divergence, (d) 2-dimensional convergence at a low pressure system, (e) 1-dimensional trough convergence, (f) frontal step convergence, and (g) convergence/divergence dipole typical of thunderstorm activitiy. (After Vachalek, et al., 1988).

We learned in this chapter that the ML has a well-defined top, and is usually in quasi-equilibrium with the surface forcings. These factors allowed us to describe relatively simple models for ML characteristics and evolution. In the next chapter, however, we will learn that the stable boundary layer has a poorly-defined top, and is rarely in equilibrium with the surface. As a result, Chapter 12 reviews other techniques that can be used to describe the stable boundary layer. Clouds, which can be a part of either stable or convective boundary layers, are described in Chapter 13.

11.6 References

Agee, E.M., 1984: Observations from space and thermal convection: a historical perspective. *Bull. Am. Meteor. Soc.*, **65**, 938-949.

Agee, E.M., T.S. Chen and K.E. Dowell, 1973: A review of mesoscale cellular

convection. *J. Appl. Meteor.*, **13**, 46-53.

André, J.-C., J.-P. Goutorbe, and A. Perrier, 1986: HAPEX-MOBILHY, a hydrologic atmospheric pilot experiment for the study of water budget and evaporation flux at the climatic scale. *Bull. Am. Meteor. Soc.*, **67**, 138-144.

Arritt, R.W., 1987: Effect of water surface temperature on lake breezes and thermal internal boundary layers. *Bound.-Layer Meteor.*, **40**, 101-125.

Atlas, D., B. Walter, S.-H. Chou and P.J. Sheu, 1986: The structure of the unstable marine boundary layer viewed by lidar and aircraft observations. *J. Atmos. Sci.*, **43**, 1301-1318.

Bader, D.C., T.B. McKee and G.J. Tripoli, 1987: Mesoscale boundary layer evolution over complex terrain. Part 1. Numerical simulation of the diurnal cycle. *J. Atmos. Sci.*, **44**, 2823-2838.

Ball, F.K., 1960: Control of inversion height by surface heating. *Quart. J. Roy. Meteor. Soc.*, **86**, 483-494.

Bénech, B., J. Noilhan, A. Druilhet, J.M. Brustet and C. Charpentier, 1986: Experimental study of an artificial thermal plume in the boundary layer. Part 1. Flow characteristics near the heat source. *J. Clim. Appl. Meteor.*, **25**, 418-437.

Boers, R. and E.W. Eloranta, 1986: Lidar measurements of the atmospheric entrainment zone and the potential temperature jump across the top of the mixed layer. *Bound.-Layer Meteor.*, **34**, 357-375.

Boers, R., E.W. Eloranta and R.L. Coulter, 1984: Lidar observations of mixed layer dynamics: Tests of parameterized entrainment models of mixed layer growth rate. *J. Clim. Appl. Meteor.*, **23**, 247-266.

Brown, R.A., 1970: A secondary flow model for the planetary boundary layer. *J. Atmos. Sci.*, **27**, 742-757.

Brutsaert, W., 1987: Nearly steady convection and the boundary layer budgets of water vapor and sensible heat. *Bound.-Layer Meteor.*, **39**, 283-300.

Carruthers, D.J. and C.-H. Moeng, 1987: Waves in the overlying inversion of the convective boundary layer. *J. Atmos. Sci.*, **44**, 1801-1808.

Chang, H.-R. and H.N. Shirer, 1984: Transitions in shallow convection: an explanation for lateral cell expansion. *J. Atmos. Sci.*, **41**, 2334-2346.

Clark, T.L., T. Hauf and J.P. Kuettner, 1986: Convectively forced internal gravity waves: results from two-dimensional numerical experiments. *Quart. J. Roy. Meteor. Soc.*, **112**, 899-925.

Crum, T.D. and R.B. Stull, 1987: Field measurements of the amount of surface layer air versus height in the entrainment zone. *J. Atmos. Sci.*, **44**, 2743-2753.

Crum, T.D., R.B. Stull and E.W. Eloranta, 1987: Coincident lidar and aircraft observations of entrainment into thermals and mixed layers. *J. Clim. Appl. Meteor.*, **26**, 774-788.

Deardorff, J.W., 1969: Numerical study of heat transport by internal gravity waves above a growing unstable layer. *Phys. Fluids, Suppl. II*, **12**, 184-194.

Deardorff, J.W., 1972: Numerical investigation of neutral and unstable planetary boundary layers. *J. Atmos. Sci.*, **29**, 91-115.

Deardorff, J.W., 1974: Three-dimensional numerical study of turbulence in an entraining

mixed layer. *Bound-Layer. Meteor.*, **7**, 199-226.

Deardorff, J.W., 1979: Prediction of convective mixed-layer entrainment for realistic capping inversion structure. *J. Atmos. Sci.*, **36**, 424-436.

Deardorff, J.W. and G.E. Willis, 1985: Further results from a laboratory model of the convective planetary boundary layer. *Bound.-Layer Meteor.*, **32**, 205-236.

Deardorff, J.W., G.E. Willis and D.K. Lilly, 1969: Laboratory investigation of non-steady penetrative convection. *J. Fluid Mech.*, **35**, 7-31.

Deardorff, J.W., G.E. Willis and B.H. Stockton, 1980: Laboratory studies of the entrainment zone of a convectively mixed layer. *J. Fluid Mech.*, **100**, Part 1, 41-64.

Doviak, R.J. and M. Berger, 1980: Turbulence and waves in the optically clear planetary boundary layer resolved by dual-Doppler radar. *Radio Science*, **15**, 297-317.

Driedonks, A.G.M. and H. Tennekes, 1984: Entrainment effects in the well-mixed atmospheric boundary layer. *Bound.-Layer Meteor.*, **30**, 75-105.

Fairall, C.W., 1987: A top-down and bottom-up diffusion model of c_T2 and c_q2 in the entraining convective boundary layer. *J. Atmos. Sci.*, **44**, 1009-1017.

Ferrare, R.A., 1984: Lidar observations of organized convection within the atmospheric mixed layer. M.S. Thesis. Dept. of Meteorology, Univ. of Wisconsin-Madison. 204pp.

Fiedler, B.H., 1984: The mesoscale stability of entrainment into cloud-topped mixed layers. *J. Atmos. Sci.*, **41**, 92-101.

Fitzjarrald, D.E., 1973: A field investigation of dust devils. *J. Appl. Meteor.*, **12**, 808-813.

Fritz, R.B. and T.-I. Wang, 1979: Chapt. 9. Optical systems measuring surface-level convergence during PHOENIX, *Project PHOENIX, Report No. 1.* (Hooke, Ed.), 57-73. Available from NOAA.ERL, Boulder, CO 80303.

Godowitch, J.M., 1986: Characteristics of vertical turbulence velocity in the urban convective boundary layer. *Bound.-Layer Meteor.*, **35**, 387-407.

Greenhut, G.K. and S.J.S. Khalsa, 1982: Updraft and downdraft events in the atmospheric boundary layer over the equatorial Pacific Ocean. *J. Atmos. Sci.*, **39**, 1803-1818.

Greenhut, G.K. and S.J.S. Khalsa, 1987: Convective elements in the marine atmospheric boundary layer. Part 1: Conditional sampling statistics. *J. Clim. Appl. Meteor.*, **26**, 813-822.

Haines, D.A., 1982: Horizontal roll vortices and crown fires. *J. Clim. Appl. Meteor.*, **21**, 751-763.

Hanna, S.R., 1987: An empirical formula for the height of the coastal internal boundary layer. *Bound.-Layer Meteor.*, **40**, 205-207.

Hooper, W.P., 1982: *The Diurnal Evolution of the Planetary Boundary Layer: Lidar Observations above a Flat Homogeneous Surface.* M.S. Thesis, Univ. of Wisconsin - Madison. 160pp.

Hooper, W.P. and E.W. Eloranta, 1986: Lidar measurements of wind in the planetary boundary layer: the method, accuracy and results from joint measurements with radiosonde and kytoon. *J. Clim. Appl. Meteor.*, **25**, 990-1001.

Hsu, S.A., 1986: A note on estimating the height of the convective internal boundary layer near shore. *Bound.-Layer Meteor.*, **35**, 311-316.

Idso, S.B., 1975: Tornado-like dust devils. *Weather*, **30**, 115-117.

Idso, S.B., 1975: Arizona weather watchers: past and present. *Weatherwise*, **28**, 56-60.

Idso, S.B., 1975: Whirlwinds, density currents, and topographic disturbances: a meteorological melange of intriguing interactions. *Weatherwise*, **28**, 61-65.

Kaimal, J.C. and J.A. Businger, 1970: Case studies of a convective plume and a dust devil. *J. Appl. Meteor.*, **9**, 612-620.

Kaimal, J.C., W.L. Eberhard, W.R. Moniger, J.E. Gaynor, S.W. Troxel, T. Uttal, G.A. Briggs, and G.E. Start, 1986: *Project Condors, Convective Diffusion observed by remote sensors*. NOAA/ERL, Boulder, CO 80303.

Khalsa, S.J.S. and G.K. Greenhut, 1985: Conditional sampling of updrafts and downdrafts in the marine atmospheric boundary layer. *J. Atmos. Sci.*, **42**, 2550-2562.

Khalsa, S.J.S. and G.K. Greenhut, 1987: Convective elements in the marine atmospheric boundary layer. Part 2: Entrainment at the capping inversion. *J. Clim. Appl. Meteor.*, **26**, 824-836.

Kraus, E.B., 1972: *Atmosphere-Ocean Interaction*. Cambridge Univ. Press., Oxford. 275pp.

Kraus, E.B. and L.D. Leslie, 1982: The interactive evolution of the oceanic and atmospheric boundary layers in the source regions of the trades. *J. Atmos. Sci.*, **39**, 2760-2772.

Kropfli, R.A., 1979: Chapt. 3. PHOENIX multiple Doppler radar operations. *Project PHOENIX - Report No. 1*. (Hooke, Ed.), 33-56. Available from NOAA/ERL, Boulder, CO 80303.

Kuettner, J.P., P.A. Hildebrand and T.L. Clark, 1987: Convection waves: observations of gravity wave systems over convectively active boundary layers. *Quart. J. Roy. Meteor. Soc.*, **113**, 445-468.

Lamb, R.G., 1978: A numerical simulation of dispersion from an elevated point source in the convective planetary boundary layer. *Atmos. Environ.*, **12**, 1297-1304.

LeMone, M.A., 1973: The structure and dynamics of horizontal roll vortices in the planetary boundary layer. *J. Atmos. Sci.*, **30**, 1077-1091.

LeMone, M.A., 1976: Modulation of turbulence energy by longitudinal rolls in an unstable planetary boundary layer. *J. Atmos. Sci.*, **33**, 1308-1320.

Lenschow, D.H., 1973: Two examples of planetary boundary layer modification over the great lakes. *J. Atmos. Sci.*, **30**, 568-581.

Lenschow, D.H. and E.M. Agee, 1986: Preliminary results from the Air Mass Transformation Experiment (AMTEX). *Bull. Am. Meteor. Soc.*, **57**, 1346-1355.

Lilly, D.K., 1968: Models of cloud-topped mixed layers under a strong inversion. *J. Atmos. Sci.*, **30**, 1092-1099.

Lyons, W.A., 1975: Turbulent diffusion and pollutant transport in shoreline environments. *Lectures on Air Pollution and Environmental Impact Analysis*, D.A. Haugen (Ed.), Am. Meteor. Soc. 136-208.

Mahrt, L., 1979: Penetrative convection at the top of a growing boundary layer. *Quart.*

J. Roy. Meteor. Soc., **105**, 469-485.

Mahrt, L. and J.-C. André, 1983: On the stratification of turbulent mixed layers. *J. Geophys. Res.*, **88**, 2662-2666.

Mahrt, L. and J. Paumier, 1984: Heat transport in the atmospheric boundary layer. *J. Atmos. Sci.*, **41**, 3061-3075.

Mahrt, L. and J. Paumier, 1985: Simple formulation of heat flux in the unstable atmospheric boundary layer. *Bound.-Layer Meteor.*, **33**, 61-76.

Mason, P.J. and R.I. Sykes, 1980: A 2-D numerical study of horizontal roll vortices in the neutral atmospheric boundary layer. *Quart. J. Roy. Meteor. Soc.*, **106**, 351-336.

Mason, P.J. and R.I. Sykes, 1982: A 2-D numerical study of horizontal roll vortices in an inversion-capped planetary boundary layer. *Quart. J. Roy. Meteor. Soc.*, **108**, 801-823.

Moeng, C.-H. and J.C. Wyngaard, 1984: Statistics of conservative scalars in the convective boundary layer. *J. Atmos. Sci.*, **41**, 3161-3169.

News and Notes, 1976: Dust devil wind velocities. *Bull. Am. Meteor. Soc.*, **57**, 600.

Nieuwstadt, F.T.M. and R.A. Brost, 1986: The decay of convective turbulence. *J. Atmos. Sci.*, **43**, 532-546.

Nieuwstadt, F.T.M. and H. van Dop, 1982: *Atmospheric Turbulence and Air Pollution Modelling*. Reidel Publ. Co., Dordrecht. 358pp.

Noilhan, J. and B. Bénech, 1986: Experimental study of an artificial thermal plume in the boundary layer. Part 3: Dynamic structure within the plume. *J. Clim. Appl. Meteor.*, **25**, 458-467.

Noilhan, J., B. Bénech, G. Letrenne, A. Druilhet and A. Saab, 1986: Experimental study of an artificial thermal plume in the boundary layer. Part 2: Some aspects of the plume thermodynamical structure. *J. Clim. Appl. Meteor.*, **25**, 439-457.

Rabin, R.M., R.J. Doviak and A. Sundara-Rajan, 1982: Doppler radar observations of momentum flux in a cloudless convective layer with rolls. *J. Atmos. Sci.*, **39**, 851-863.

Randall, D.A., 1984: Buoyant production and consumption of turbulence kinetic energy in cloud-topped mixed layers. *J. Atmos. Sci.*, **41**, 402-413.

Ray, D., 1986: Variable eddy diffusivities and atmospheric cellular convection. *Bound.-Layer Meteor.*, **36**, 117-131.

Rayment, R. and C.J. Readings, 1974: A case study of the structure and energetics of an inversion. *Quart. J. Roy. Meteor. Soc.*, **100**, 221-223.

Reichmann, H., 1975: *Cross-country Soaring (Streckensegelflug)*. Thompson Publications. P.O. Box 1175, Pacific Palisades, CA 90272. 150pp.

Reinking, R.F., R.J. Doviak and R.O. Gilmer, 1981: Clear-air roll vortices and turbulent motions as detected with an airborne gust probe and dual-Doppler radar. *J. Appl. Meteor.*, **20**, 678-685.

Rosmond, T.E., 1973: Mesoscale cellular convection. *J. Atmos. Sci.*, **30**, 1392-1409.

Rothermal, J. and E.M. Agee, 1980: Aircraft investigation of mesoscale cellular convection during AMTEX 75. *J. Atmos. Sci.*, **37**, 1027-1040.

Rothermel, J. and E.M. Agee, 1986: A numerical study of atmospheric convective scaling. *J. Atmos. Sci.*, **43**, 1185-1197.

Schols, J.L.J., 1984: The detection and measurement of turbulent structures in the atmospheric surface layer. *Bound.-Layer Meteor.*, **29**, 39-58.

Schols, J.L.J., A.E. Jansen and J.G. Krom, 1985: Characteristics of turbulent structures in the unstable atmospheric surface layer. *Bound.-Layer Meteor.*, **33**, 173-196.

Schols, J.L.J. and L. Wartena, 1986: A dynamical description of turbulent structure in the near neutral atmospheric surface layer: the role of static pressure fluctuations. *Bound.-Layer Meteor.*, **34**, 1-15.

Scorer, R.S., 1957: Experiments on convection of isolated masses of buoyant fluid. *J. Fluid Mech.*, **2**, 583-594.

Sheu, P.J. and E.M. Agee, 1977: Kinematic analysis and air-sea heat flux associated with mesoscale cellular convection during AMTEX 75. *J. Atmos. Sci.*, **34**, 793-801.

Sinclair, P.C., V.H. Leverson and R.F. Abbey, Jr., 1977: The vortex structure of dust devils, water spouts, and tornadoes. *10th AMS Conference on Severe Local Storms, Oct 18-21, Omaha, NE.* Amer. Meteor. Soc., Boston. 533pp.

Smolarkiewicz, P.K. and T.L. Clark, 1985: Numerical simulation of the evolution of a three-dimensional field of cumulus clouds. Part 1: Model description, comparison with observations and sensitivity studies. *J. Atmos. Sci.*, **42**, 502-522.

Stage, S.A. and J.A. Businger, 1981: A model for entrainment into a cloud-topped marine boundary layer. Parts 1 & 2. *J. Atmos. Sci.*, **38**, 2213-2242.

Stull, R.B., 1973: Inversion rise model based on penetrative convection. *J. Atmos. Sci.*, **30**, 1092-1099.

Stull, R.B., 1976a: The energetics of entrainment across a density interface. *J. Atmos. Sci.*, **33**, 1260-1267.

Stull, R.B., 1976b: Mixed layer depth model based on turbulent energetics. *J. Atmos. Sci.*, **33**, 1268-1278.

Stull, R.B., 1976c: Internal gravity waves generated by penetrative convection. *J. Atmos. Sci.*, **33**, 1279-1286.

Stull, R.B., 1985: A fair-weather cumulus cloud classification scheme for mixed-layer studies. *J. Clim. Appl. Meteor.*, **24**, 49-56.

Stull, R.B., 1988: Pollutant dispersion and mixed-layer modeling using asymmetric transilient matrices. 8th AMS Symposium on Turbulence and Diffusion. San Diego, 25-29 April 1988. Amer. Meteor. Soc., Boston. 4pp.

Stull, R.B. and A.G.M. Driedonks, 1987: Applications of the transilient turbulence parameterization to atmospheric boundary-layer simulations. *Bound.-Layer Meteor.*, **40**, 209-239.

Tennekes, H., 1973: A model for the dynamics of the inversion above a convective boundary layer. *J. Atmos. Sci.*, **30**, 558-581.

Vachalek, R.E., R.B. Stull, and E.W. Eloranta, 1988: Mean vertical velocity and divergence measurements in the boundary layer. (Submitted to J. Appl. Meteor.)

Venkatram, A., 1977: A model for internal boundary layer development. *Bound.-Layer Meteor.*, **11**, 419-437.

Weinstock, J., 1987: The turbulence field generated by a linear gravity wave. *J. Atmos.*

Sci., **44**, 410-420.

Wilczak, J.M. and J.A. Businger, 1983: Thermally indirect motions in the convective atmospheric boundary layer. *J. Atmos. Sci.*, **40**, 343-358.

Wilczak, J.M. and J.E. Tillman, 1980: The three-dimensional structure of convection in the atmospheric surface layer. *J. Atmos. Sci.*, **37**, 2424-2443.

Wilde, N.P., R.B. Stull, and E.W. Eloranta, 1985: The LCL zone and cumulus onset. *J. Clim. Appl. Meteor.*, **24**, 640-657.

Willis, G.E. and J.W. Deardorff, 1976: A laboratory model of diffusion into the convective planetary boundary layer. *Quart. J. Roy. Meteor. Soc.*, **102**, 427-445.

Willis, G.E. and J.W. Deardorff, 1978: A laboratory study of dispersion from an elevated source within a modeled convective planetary boundary layer. *Atmos. Environ.*, **12**, 1305-1311.

Willis, G.E. and J.W. Deardorff, 1981: A laboratory study of dispersion from a source in the middle of the convectively mixed layer. *Atmos. Environ.*, **15**, 109-117.

Wyngaard, J.C., 1987: A physical mechanism for the asymmetry in top-down and bottom-up diffusion. *J. Atmos. Sci.*, **44**, 1083-1087.

Wyngaard, J.C. and R.A. Brost, 1984: Top-down and bottom-up diffusion of a scalar in the convective boundary layer. *J. Atmos. Sci.*, **41**, 102-112.

Young, G.S., 1988a&b: Turbulence structure of the convective boundary layer. Parts I & II. *J. Atmos. Sci.*, **44**, (in press).

Young, G.S., 1988c: Convection in the atmospheric boundary layer. *Earth Science Reviews* (in press).

11.7 Exercises

1) Given a ML that is initially 500 m thick with an average virtual potential temperature $<\overline{\theta_v}> = 280$ K. Assume that the mixed layer depth, z_i, and $<\overline{\theta_v}>$ change with time according to: $dz_i/dt = w_e$ and $d<\overline{\theta_v}>/dt = [\overline{w'\theta_v'}_s - \overline{w'\theta_v'}_{z_i}] / z_i$ where the entrainment velocity, $w_e = 0.01$ m/s. At the top of the mixed layer is a sharp (step) inversion, above which $\overline{\theta_v} = 292$ K and is constant with height. This mixed layer is over a warm ocean,having a sea surface temperature of $<\overline{\theta_v}>_s = 290$ K. This temperature remains constant with time, both day and night. Assume that the mean wind speed is $\overline{M} = 5$ m/s and is constant with time, and that the bulk transfer coefficient is $C_H = 0.002$.

a) Find an equation for $<\overline{\theta_v}>$ as a function of time.

b) Plot your answer over a 30 h period.

c) Assume the mixed layer remains well mixed as it grows in thickness. Plot $\overline{w'\theta_v'}$ vs. z at the initial time (t = 0).

2) Given the following sounding at sunrise: $\overline{\theta_v} = a - b \exp(-z/c_1)$, where a = 300 K, b = 10 K, and $c_1 = 100$ m. Use the thermodynamic (encroachment) approach to find and plot the ML depth, z_i , as a function of time, t, since sunrise (out to 6 h), given $\overline{w'\theta_v'}_s = c_2 \sin(\pi t / 12h)$, where $c_2 = 0.3$ K m/s. Assume no subsidence.

3) Given a slab-like ML with mean properties < > , capped by a discontinuity of Δ( ), where: $z_i = 1000$ m, no subsidence, $<\overline{\theta_v}> = 300$ K, $<\overline{U}> = 5$ m/s, $\Delta\overline{\theta_v} = 1$ K, $\Delta\overline{U} = 2$ m/s, $\partial\overline{\theta_v}/\partial z = 5$ K/km above the discontinuity, $\overline{w'\theta_v'}_s = 0.2$ K m/s, and $u_* = 0.35$ m/s.

a) Calculate the entrainment velocity, w_e, using the (1) flux-ratio approach, and (2) energetics approach.

b) If $\overline{w'\theta_v'}_s$ = constant with time, then use the flux ratio approach to calculate and plot

z_i, $\langle \overline{\theta_v} \rangle$, and w_e as a function of time for a 3 h period.

c) If the entrainment-zone thickness, Δh equals 0.3 z_i , and the lifting condensation level (LCL) is at a constant height of 1500 m, then when will the first convective clouds form? Use the results from part (b).

4) Given the steady-state advection of cold air from land over warmer water, write the equation set necessary to find the change in height of the internal boundary layer (i.e., the new ML forming over the warmer water) as a function of distance downwind from the shore. Do NOT solve these equations, just write the equations without solution, but simplified as much as possible.

Assume: The initial cold air from the land has a uniform lapse rate, γ. You can use the flux ratio approach to determine the new ML depth over water. Align the coordinate system with the mean wind. Assume lateral homogeneity (i.e., no crosswind), neglect subsidence, and neglect $\overline{u'\theta'}$. Assume the water surface temperature, θ_G, is constant in time and space. Assume the mean wind speed and direction are constant with height. Neglect radiation and latent heating.

5) If the moisture flux at z_i is $\rho\overline{w'q'} = 0.10\ g_{water}\ m^{-2}s^{-1}$, and $\Delta\overline{q} = -5\ g_{water}/kg_{air}$, and $\Delta\overline{\theta} = 3$ K, then:

a) Find the value of entrainment velocity (w_e).

b) Find the value of heat flux (in kinematic units) at z_i.

6) Given a dry convective mixed layer with initial conditions $z_i = 500$ m, and $\Delta\overline{\theta} = 5$ K, as sketched below. Assume the surface heat flux is $\overline{w'\theta'}_s = 0.2$ K m/s and is constant with time. Use the flux ratio approach. Remember that $\partial(\Delta\overline{\theta})/\partial t = \gamma\, w_e - \partial\langle\overline{\theta}\rangle/\partial t$, where γ is the lapse rate in the free atmosphere.

a) What must the subsidence be initially to prevent the mixed layer from rising (i.e., z_i = constant = 500 m)?

b) How must the subsidence vary with time over a 3 h period to prevent the mixed layer from rising? Plot your result in a graph like the one shown below.

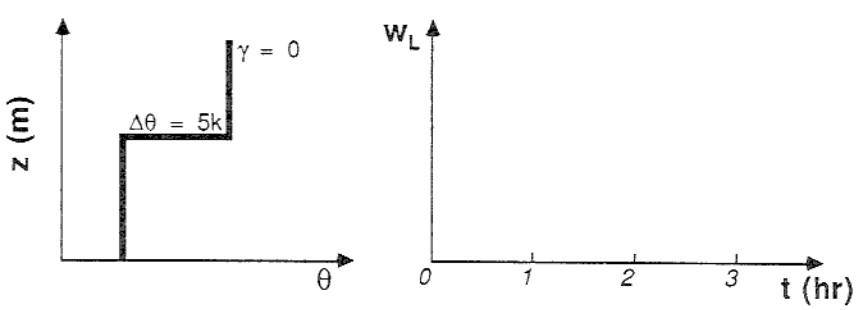

7) Given the initial sounding at $t_o = 0600$ local time as plotted below. Assume that the sensible heat flux varies with time over this land surface according to:

$\overline{w'\theta'} = c_1 \cdot \sin[\pi\ (t-t_o)/\ c_2\ ]$, where $c_1 = 0.2$ K m s^{-1}, and $c_2 = 12$ h. Use the thermodynamic (encroachment) approach to estimate the mixed layer depth (z_i) and mean potential temperature $\langle\overline{\theta}\rangle$ at $t = 1800$ local time.

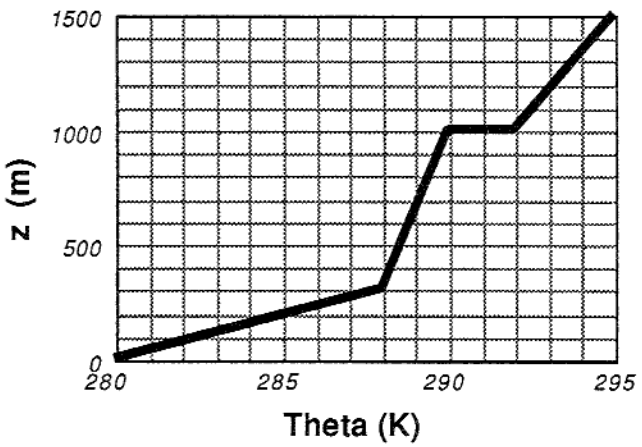

8) What do the surface-layer plume and dust devil have in common?

9) If the initial lapse rate at sunrise is linear (with $\partial\overline{\theta}/\partial z = 10$ K/km and a surface temperature of $\overline{\theta} = 10°C$), and if the total heat input from sunrise to 10 AM is 10^3 m·K, then use the thermodynamic method to estimate z_i at 10 AM.

10) List all the kinds and scales of buoyancy waves that are observed near the entrainment zone and lower FA.

11) Suppose that a slab ML has an initial depth $z_i = 100$ m and an initial temperature of $\overline{\theta} = 280$ K. This air is advecting from land to warmer water ($\overline{\theta} = 290$ K) with a mean wind speed of $\overline{M} = 5$ m/s. Over land, there is no flux into the bottom of the ML and no entrainment into the top. Over water, the flux at the bottom can be approximated with a bulk transfer relationship (use $C_D = C_H = 10^{-3}$ as the bulk transfer coefficient). The flux ratio method can be used to model entrainment at the top of the ML. (Neglect subsidence, and assume that the inversion capping the ML has a constant strength of $\Delta\overline{\theta} = 2$ K.) How do the thickness and temperature measured 1 km downwind from the shoreline vary with speed (your answer can be in word and/or equation form, although no numbers need be found)?

12) If an air parcel rises through the mixed layer and penetrates into the entrainment zone with an initial vertical velocity at the base of the inversion of 5 m/s and initial temperature equal to the ML temperature of $\overline{\theta}$ = 300 K, how far will the parcel overshoot, if:
   a) the temperature step at the top of the ML is 3 K and the lapse rate in the FA is adiabatic?
   b) there is no temperature step at the Ml top, but there is a constant lapse rate of $\partial\overline{\theta}/\partial z$ = 5 K/km?
13) How do surface layer plumes relate to updraft curtains and convergence lines?
14) Suppose that the FA is filled with high concentrations of a tracer called BSP (blue sky pigment). This tracer is entrained into the top of the ML with flux $\overline{w'c'}_{z_i}$ = - 0.1 g m/s. This tracer is lost from the bottom of the ML by being absorbed into lakes (causing blue lakes) at the same rate: $\overline{w'c'}_s$ = - 0.1 g m/s. Use top-down bottom-up methods to calculate and plot the shape of the mean concentration, $\overline{C}$, of BSP as a function of height, z/z_i, in the ML. What is the mean gradient across the ML? Do the calculations for: a) w_* = 2 m/s. b) w_* = 0.2 m/s.
15) How would smoke disperse from a 200 m high smoke stack if the ML were 800 m thick, and if the vertical velocity frequency distribution were positively skewed (instead of the negatively skewed distribution that is observed in nature)?
16) What are the similarities and differences between the entrainment zone and the intromission zone?
17) For a 1 km thick boundary layer with a 3 K potential temperature difference across it, what is the value of
   a) the Rayleigh number for air?
   b) the turbulent Rayleigh number for air (and state assumptions for K)?
18) Find and plot Δh vs. time for a 3 h period. Assume for simplicity that the average ML top, z_i, occurs in the middle of the entrainment zone. Suppose $z_i = a \cdot t^{1/2}$, and $\Delta\overline{\theta} = b \cdot (t+c)^{-1/2}$, where a = 8.333 m $s^{-1/2}$, b = 180 K $s^{1/2}$, and c = 1 h. Assume the air is dry, and the surface flux is constant at $\overline{w'\theta'}$ = 0.2 K m/s, and $g/\overline{\theta}$ = 0.03333 m s^{-2} K^{-1}.
19) If a ML grows approximately 1 km during a 12 h period, calculate the average entrainment velocity. Is it possible to have great enough subsidence to oppose the ML growth? If so, which horizontal scale would be most likely to support subsidence of that magnitude?